iScience

CellPress
OPEN ACCESS

Article

Hyperphosphorylation of hepatic proteome characterizes nonalcoholic fatty liver disease in S-adenosylmethionine deficiency

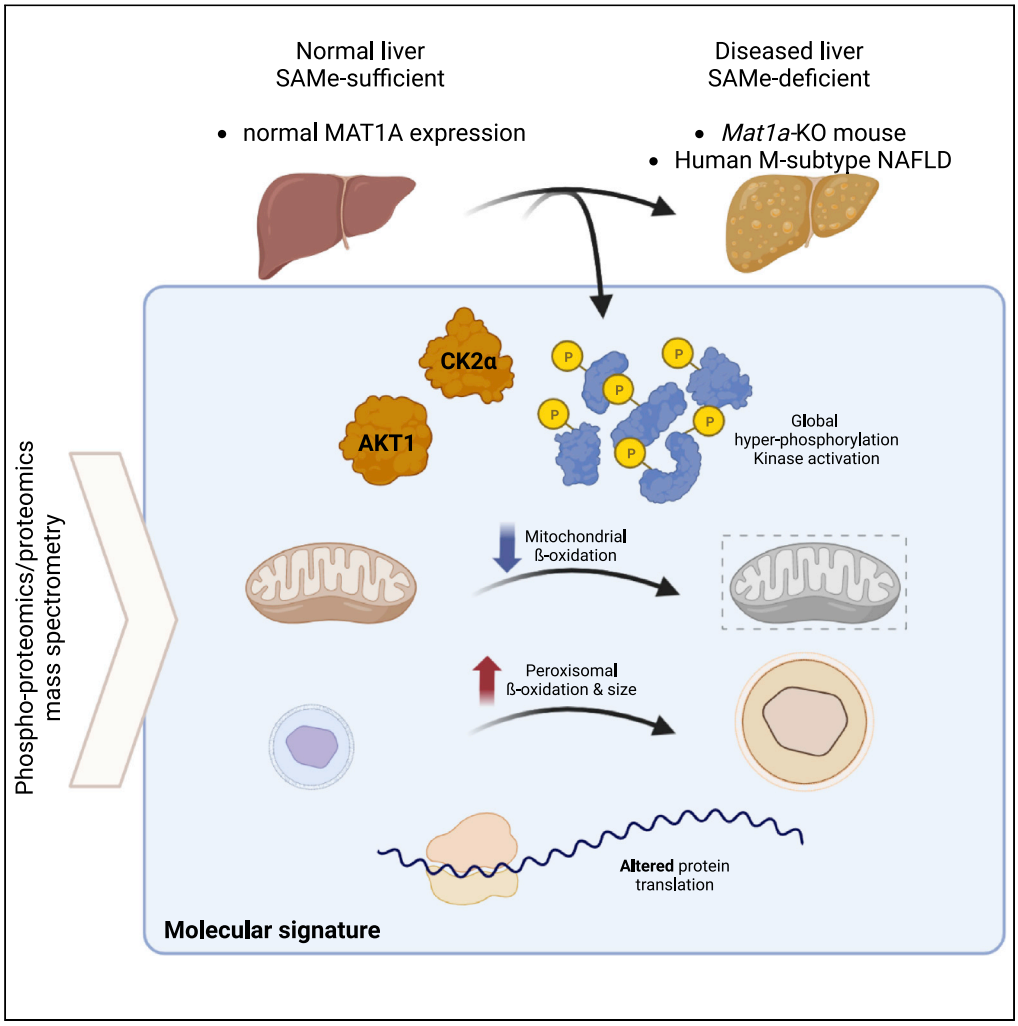

Aaron E. Robinson, Aleksandra Binek, Komal Ramani, ..., José M. Mato, Shelly C. Lu, Jennifer E. Van Eyk

jennifer.vaneyk@cshs.org (S.C.L.)
shelly.lu@cshs.org (J.E.V.E.)

Highlights

SAMe deficiency in mouse and human NAFLD causes hyperphosphorylation in the liver

Hyperphosphorylation correlates with activation of the kinases, CK2α and AKT1

SAMe deficiency alters mitochondrial, peroxisomal, and protein translation pathways

SAMe-deficient phosphoproteome signature may be therapeutically relevant in NAFLD

Robinson et al., iScience 26, 105987
February 17, 2023 © 2023
https://doi.org/10.1016/j.isci.2023.105987

iScience

CellPress
OPEN ACCESS

Article

Hyperphosphorylation of hepatic proteome characterizes nonalcoholic fatty liver disease in S-adenosylmethionine deficiency

Aaron E. Robinson,[1,4] Aleksandra Binek,[1,4] Komal Ramani,[2,4] Niveda Sundararaman,[1] Lucía Barbier-Torres,[2] Ben Murray,[2] Vidya Venkatraman,[1] Simion Kreimer,[1] Angela Mc Ardle,[1] Mazen Noureddin,[2] David Fernández-Ramos,[3] Fernando Lopitz-Otsoa,[3] Virginia Gutiérrez de Juan,[3] Oscar Millet,[3] José M. Mato,[3] Shelly C. Lu,[2,*] and Jennifer E. Van Eyk[1,5,*]

SUMMARY

Methionine adenosyltransferase 1a (MAT1A) is responsible for hepatic S-adenosyl-L-methionine (SAMe) biosynthesis. *Mat1a*$^{-/-}$ mice have hepatic SAMe depletion, develop nonalcoholic steatohepatitis (NASH) which is reversed with SAMe administration. We examined temporal alterations in the proteome/phosphoproteome in pre-disease and NASH *Mat1a*$^{-/-}$ mice, effects of SAMe administration, and compared to human nonalcoholic fatty liver disease (NAFLD). Mitochondrial and peroxisomal lipid metabolism proteins were altered in pre-disease mice and persisted in NASH *Mat1a*$^{-/-}$ mice, which exhibited more progressive alterations in cytoplasmic ribosomes, ER, and nuclear proteins. A common mechanism found in both pre-disease and NASH livers was a hyperphosphorylation signature consistent with casein kinase 2α (CK2α) and AKT1 activation, which was normalized by SAMe administration. This was mimicked in human NAFLD with a metabolomic signature (M-subtype) resembling *Mat1a*$^{-/-}$ mice. In conclusion, we have identified a common proteome/phosphoproteome signature between *Mat1a*$^{-/-}$ mice and human NAFLD M-subtype that may have pathophysiological and therapeutic implications.

INTRODUCTION

Nonalcoholic fatty liver disease (NAFLD) has emerged as the most common cause of chronic liver disease with worldwide prevalence of 25% that reflects the global rise in obesity.[1] NAFLD encompasses a spectrum, from simple steatosis to nonalcoholic steatohepatitis (NASH), a condition characterized by the concordance of steatosis with liver injury, inflammation, and fibrosis.[1–3] Roughly 25% of patients with NAFLD have NASH,[3] of whom 25% can progress to liver cirrhosis, of whom 1%–2% will develop hepatocellular carcinoma in their lifetime.[3] There are currently no FDA-approved treatments for NASH, and consequently, NASH has recently overtaken hepatitis C as the most common indication for liver transplantation for woman in the United States, highlighting the need for a viable treatment for this major public health problem.[4,5]

To understand disease progression of NASH in humans as well as to identify molecular targets involved in the disease progression, murine models are commonly used as they mimic some but not all aspects of human disease.[6,7] Recent work has shown that nearly half of patients with NAFLD have a serum metabolomic profile (M-subtype) that closely resembles the methionine adenosyltransferase 1a knockout mouse (*Mat1a*$^{-/-}$) model.[8] Prior to any histological signs of disease, four-month-old *Mat1a*$^{-/-}$ mice (pre-disease *Mat1a*$^{-/-}$) are more susceptible to diet-induced liver steatosis.[9] By eight months of age, *Mat1a*$^{-/-}$ mice spontaneously develop NASH (*Mat1a*$^{-/-}$ NASH), which can be reversed by exogenous S-adenosyl-L-methionine (SAMe) administration histologically and biochemically.[8,9] SAMe is the principal methyl donor responsible for DNA, RNA, and protein methylation.[10] In the liver, majority of the biosynthesis of SAMe is via *MAT1A*-encoded isoenzyme while *MAT2A* synthesizes SAMe in non-hepatic tissues.[11] In the *Mat1a*$^{-/-}$ NASH model, kinase/phosphatase signaling is dysregulated but the impact on protein phosphorylation (and the proteome) is unknown. *Mat1a*$^{-/-}$ animals have higher activity of ERK2,[12] LKB1,[13,14] AKT,[14] and

[1]Advanced Clinical Biosystems Research Institute, The Smidt Heart Institute, Cedars Sinai Medical Center, Advanced Health Sciences Pavilion, 127 S. San Vicente Blvd, Room 9302, Los Angeles, CA 90048, USA

[2]Karsh Division of Gastroenterology and Hepatology, Cedars-Sinai Medical Center, 8700 Beverly Blvd, Davis Building, Room 2097, Los Angeles, CA 90048, USA

[3]CIC bioGUNE, Centro de Investigación Biomédica en Red de Enfermedades Hepáticas y Digestivas (Ciberehd), Technology Park of Bizkaia, 48160 Derio, Bizkaia, Spain

[4]These authors contributed equally

[5]Lead contact

*Correspondence: jennifer.vaneyk@cshs.org (S.C.L.), shelly.lu@cshs.org (J.E.V.E.)

https://doi.org/10.1016/j.isci.2023.105987

AMPK[13,14] in addition to decreased dual-specificity MAPK phosphatase 1 (DUSP1) activity[12] suggestive of increased phosphorylation with disease. Importantly, exogenous SAMe administration normalized ERK2 and DUSP1 activity in the *Mat1a*$^{-/-}$ NASH model,[12] suggesting that SAMe administration should normalize hyperactive kinases in a SAMe-deficient system.

The goals of this study were: (1) quantify the proteome (protein quantity) and phosphoproteome (site-specific phosphorylation quantity) signatures at different stages in the progression of the *Mat1a*$^{-/-}$ NASH mouse model to gain insight into the temporal order of altered signaling pathways, (2) to identify SAMe-sensitive signatures linked to the beneficial outcome of SAMe treatment, and (3) to identify conserved disease signatures in human M-subtype human NAFLD that are also present in the *Mat1a*$^{-/-}$ model. Furthermore, early alterations during disease progression can provide clues on the initiating pathogenesis of disease and provide early biomarkers of disease. Our analyses revealed a global hyperphosphorylation that is already striking in the pre-disease *Mat1a*$^{-/-}$ livers that widely normalized after SAMe administration. The phosphoproteome revealed a hyperactive casein kinase 2α (CK2α) and AKT1 signature in the *Mat1a*$^{-/-}$ NASH model that is responsive to SAMe administration. Importantly, the same hyperphosphorylation and hyperactive CK2α and AKT1 signature were observed in human NAFLD with the M-subtype.

RESULTS

To understand the molecular underpinnings of and to identify early drivers in the *Mat1a*$^{-/-}$ NASH model, we utilized two groups of animals at, one "pre-disease" and the other with NASH (referred to as *Mat1a*$^{-/-}$ NASH). The first cohort of mice consists of *Mat1a*$^{-/-}$ mice and wild-type (WT) littermates aged four months. We showed that the livers from mice around this age are normal, but they developed massive fatty liver when challenged with a choline-free diet for only six days.[9] These mice were given 100 mg/kg/day of SAMe for seven days (Figure S1A), which we had shown normalized hepatic SAMe level in *Mat1a*$^{-/-}$ mice.[12] Histological evaluation, triglyceride levels, and alanine transaminase (ALT)/aspartate transaminase (AST) levels for this cohort are shown in Figures S1B–S1D, respectively. We also studied a cohort of *Mat1a*$^{-/-}$ animals aged ten months with NASH. This cohort includes mice given 30 mg/kg of SAMe five days a week for eight weeks starting at 8 months of age (Figure S1E). We demonstrated that SAMe administration in this cohort nearly normalized the liver histology and ALT/AST levels.[8]

To identify potential kinase and phosphatase signaling pathways and the downstream phosphorylated proteins, we performed a TiO2 phospho(tryptic) peptide affinity enrichment of both the pre-disease and NASH cohorts of *Mat1a*$^{-/-}$ animals and performed data-dependent acquisition-mass spectrometry analysis. In addition, total protein quantity was obtained through data-independent acquisition-mass spectrometry from the same samples. The results from these experiments and % fold change normalized to total protein (phosphorylation/total protein) are shown in Table 1. There was a dramatic increase in phosphorylation sites in *Mat1a*$^{-/-}$ pre-disease and NASH livers compared to age- and gender-matched WT livers with 525 and 685 phosphosites altered, which corresponded to an increase in 364 and 528 phosphoproteins, respectively (Figures 1A and 1B, Table 1). Normalizing phosphoproteome to the specific protein quantity allowed assessment of whether the changes in phosphorylation status are due to i) altered phosphorylation at specific sites, or ii) a change in the protein quantity. As shown in Table 1, regardless of disease state, majority of the changes were due to an increase in the phosphorylation at each phosphosite (90.4% and 87.9% hyperphosphorylation for *Mat1a*$^{-/-}$ pre-disease and NASH, respectively). This pathological signature corresponds to 52 hyperphosphorylated proteins in pre-disease *Mat1a*$^{-/-}$ and 148 hyperphosphorylated proteins in *Mat1a*$^{-/-}$ NASH. Raw data files of *Mat1a*$^{-/-}$ pre-disease and NASH are uploaded on (https://panoramaweb.org/Mat1a_NASH.url, ProteomeXchange ID: PXD022122, https://panoramaweb.org/Larp1.url).

Sixty of the differentially expressed hyperphosphorylated proteins in the *Mat1a*$^{-/-}$ NASH livers are established downstream phosphotargets of both CK2α and AKT1. The results are consistent with the activation of both kinases at all disease stages in the *Mat1a*$^{-/-}$ NASH model (Figures 1C and 1D), In pre-disease stage, although there was a non-significant increase in CK2α protein levels (18.3%, 11.3% false discovery rate or FDR), CK2α and AKT1 activation was predicted based on phosphoproteomics results (Figures 1C and 1D), and we quantified an increase in AKT1 Ser129 phosphorylation (157% increase, p value = 0.0073). In *Mat1a*$^{-/-}$ NASH compared to WT animals, there was an increase in CK2α protein expression (57%, 0.00001% FDR). Increased CK2α and AKT1 activity was predicted from phosphoproteomics

Table 1. Summary of phosphoproteomics

Sample Information		Phosphorylation Raw Data				Phosphorylation/Total Protein Data			
Group Comparison	Disease Stage	Total Phospho-sites Increased	Total Phospho-sites Decreased	Phospho-sites Increased (significant)	Phospho-sites Decreased (significant)	Total Phospho-sites Increased	Total Phospho-sites Decreased	Phospho-sites Increased (significant)	Phospho-sites Decreased (significant)
Mat1a$^{-/-}$ vs. WT	Pre-disease	2838	726	525	35	902	271	66	7
Mat1a$^{-/-}$ + SAMe vs. *Mat1a*$^{-/-}$	Pre-disease	1426	2210	60	112	317	909	13	116
Mat1a$^{-/-}$ vs. WT	NASH	2809	1500	685	232	1500	582	269	37
Mat1a$^{-/-}$ + SAMe vs. *Mat1a*$^{-/-}$	NASH	827	3395	117	1081	434	1526	28	303
Human M-Type vs. Non-M	NAFLD	753	161	232	20	648	470	69	41

The number of phosphosites before and after normalization to total protein levels was compared between groups of *Mat1a*−/− pre-disease/NASH and human M/non-*M*-type NASH. Significance is defined as the phosphosites in each group with $p < 0.05$.

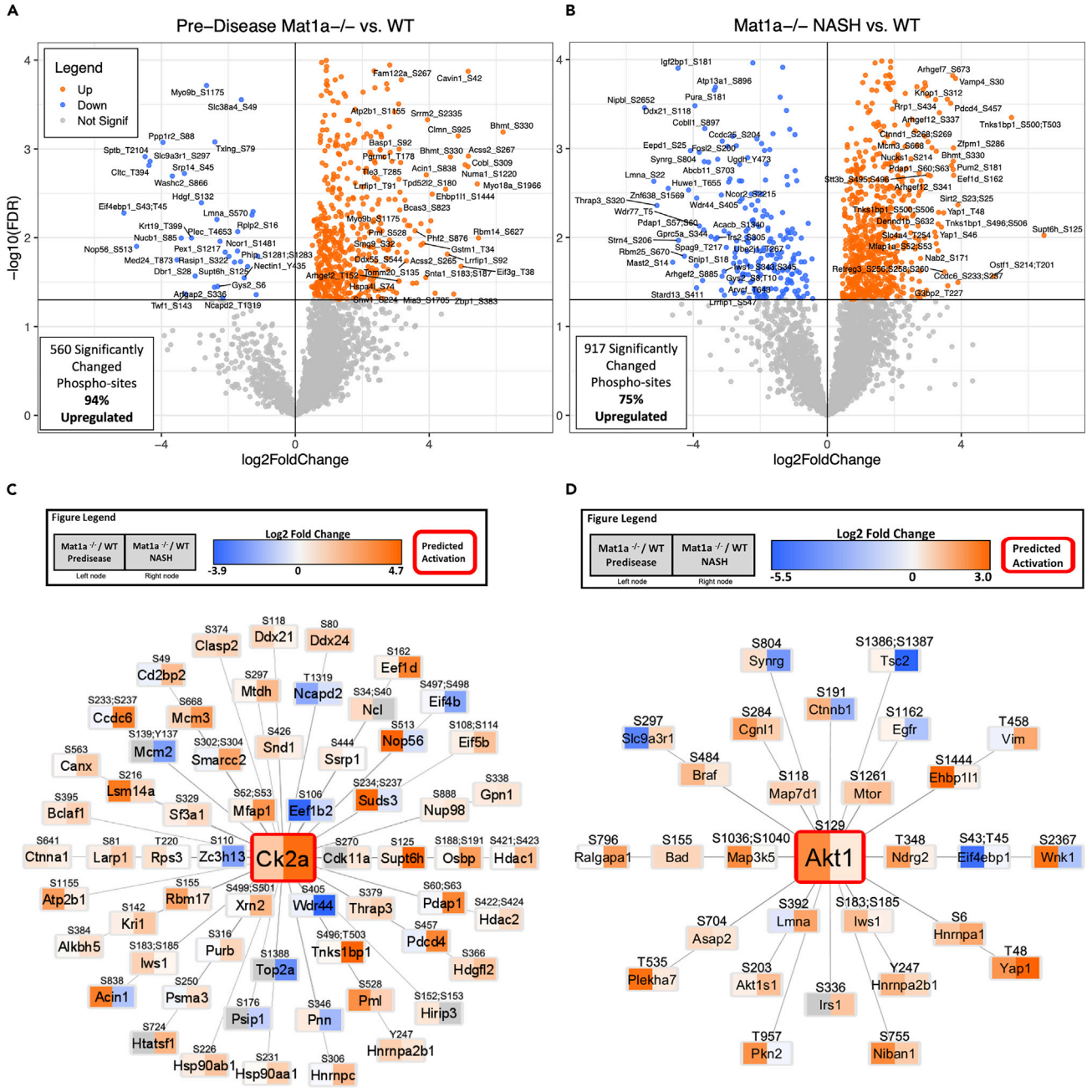

Figure 1. Phospho-proteomic changes in *Mat1a*$^{-/-}$ mice livers

(A) Phospho-proteomic changes found in pre-disease *Mat1a*$^{-/-}$ animals compared to WT littermates aged four months (n = 4/condition). 252 phosphopeptides in this comparison with a p value <0.05 and a fold change greater than 25% in either direction. Of these phosphopeptides, 236 are increased in *Mat1a*$^{-/-}$ while only 16 phosphopeptides are decreased. The X axis denotes the gene name for each protein and their corresponding phosphosite.

(B) Phosphoproteomic changes found in *Mat1a*$^{-/-}$ NASH compared to WT littermates aged ten months (n = 6/condition). 917 phosphopeptides in this comparison with a p value <0.05 and a fold change greater than 25% in either direction. Of these phosphopeptides, 685 are increased in *Mat1a*$^{-/-}$ while 232 phosphopeptides are decreased in *Mat1a*$^{-/-}$.

(C) IPA phosphorylation analysis of predicted activation status of upstream kinases through a curated database of phosphoproteomic datasets found CK2α was predicted to be activated in pre-disease *Mat1a*$^{-/-}$ (activation *Z* score = 4.49, adjusted p value = 5.88E-7) and in *Mat1a*$^{-/-}$ NASH (activation *Z* score = 3.394, adjusted p value = 2.34E-14). The left node of the bicolor node represents the pre-disease condition and the right node represents the NASH condition. The color gradient of the bicolor nodes is the range of log2-fold changes from predicted inhibition (blue gradient) to activation (orange gradient).

(D) IPA phosphorylation analysis found AKT1 was predicted to be activated in pre-disease *Mat1a*$^{-/-}$ (activation *Z* score = 2.83, adjusted p value = 1.06E-3) and in *Mat1a*$^{-/-}$ NASH (activation *Z* score = 1.149, adjusted p value = 2.61E-2). The bicolor nodes are defined as in "C" above.

(Figures 1C and 1D), although little or no AKT1 Ser129 phosphorylation in *Mat1a*$^{-/-}$ NASH was observed (39.1% increase, 0.19 p value). A well-known target of CK2α is α-Catenin, which is phosphorylated by CK2α at Ser641 residue regulating its interaction with β-catenin.[15] Both the pre-disease and NASH *Mat1a*$^{-/-}$ phosphoproteome showed a 1.4- to 1.7-fold induction in Ser641 α-catenin phosphorylation (both are significantly different from WT with $p < 0.005$) (Figure 1C).

Phosphorylation changes can be regulated by phosphatases, and within the protein quantity and phosphorylation datasets, there are several dysregulated serine, threonine, and dual specificity phosphatases which we focused on as the majority of phosphorylation changes occurred on these amino acid residues (Tables S1 and S2). There was minimal overlap in the altered phosphatases in pre-disease and *Mat1a*$^{-/-}$ NASH with only one (PPM1F) in common. Overall, there were more phosphatases inhibited than activated (4/6 and 6/8, respectively) including decreases in PPA2, MDP1, SHOC2, and PPM1F in pre-disease *Mat1a*$^{-/-}$ livers compared to respective WT controls (Table S1). In *Mat1a*$^{-/-}$ NASH, six phosphatases were decreased compared to WT (Table S2) including CPPED, a phosphatase known to deactivate AKT by dephosphorylating AKT Ser473[16] and protein phosphatase 5C (PPP5C), a known inhibitor of ASK1 through its phosphatase activity.[17]

Although the hyperphosphorylation signature was dominant in *Mat1a*$^{-/-}$ animals, there were also quantitative changes in proteins involved in lipid metabolism. Of the 411 differentially expressed proteins (Figure 2A) in pre-disease *Mat1a*$^{-/-}$, there were 24 peroxisomal proteins (adjusted p value = 2.83E-23), 6 are involved in peroxisomal lipid metabolism (adjusted p value = 6.95E-06), 25 lysosomal proteins (adjusted p value = 5.70E-13), and 141 mitochondrial proteins (adjusted p value = 8.15E-107), 10 are involved in mitochondrial fatty acid β-oxidation (adjusted p value = 2.09E-11) (Figures 2B and S2, Table S3). In *Mat1a*$^{-/-}$ animals with NASH, there is twice the number of differential proteins compared to pre-disease (921 verse 411, respectively, Figure 2C). Interestingly, there is a similar set of cellular compartments and pathways altered, specifically lipid metabolism (17.6% enrichment), 310 mitochondria proteins (adjusted p value = 4.12E-249), 12 proteins involved in mitochondrial fatty acid β-oxidation (adjusted p value = 6.74E-11) and 35 peroxisomal proteins (adjusted p value = 2.80E-29) with 11 involved in peroxisomal lipid metabolism (adjusted p value = 3.35E-11). In addition, in *Mat1a*$^{-/-}$ NASH, there was also an additional 339 nuclear proteins (adjusted p value = 3.23E-102) and 14 spliceosomal proteins (adjusted p value = 0.00005), both cellular compartments important for transcription (38 proteins, adjusted p value = 5.46E-9) and translation (98 proteins, adjusted p value = 3.20E-69) (Figures 2D and S3, Table S3). Taken together, early in disease before visible steatosis, there is already a reduction in the expression of proteins involved in mitochondrial β-oxidation and an increase in peroxisomal β-oxidation. This pattern continues with the onset of NASH. In addition, NASH also exhibits alterations in the transcriptional and translational proteome. For transcription or translation, a definitive direction could not be deciphered. However, a specific subset of ribosomal proteins and translation factors found to be responsive to the translational regulator; LARP1 were found to be induced in *Mat1a*$^{-/-}$ NASH mice as we reported previously.[18] Consistently, immunofluorescent staining in *Mat1a*$^{-/-}$ NASH livers shows increased peroxisome size without a change in number, which was normalized by SAMe treatment (Figure S6B). However, mitochondrial size and number were unchanged in the *Mat1a*$^{-/-}$ NASH livers (Figure S6C).

In pre-disease *Mat1a*$^{-/-}$ animals, although we could not detect enrichment in altered nuclear protein or proteins involved in translation, we observe changes in the phosphoproteome of these animals, which foreshadow these altered cellular compartments and pathways seen in *Mat1a*$^{-/-}$ NASH. In pre-disease *Mat1a*$^{-/-}$ animals, there are altered phosphoproteins which reside in the ribonuclear protein granule (15 proteins, adjusted p value = 9.79E-10) and involved in translation (31 proteins, adjusted p value = 1.69E-17) (Table S3) and the peroxisome (five proteins, adjusted p value = 0.012), including four peroxins which are involved in peroxisomal protein import and peroxisomal biogenesis.[20] Equally, phosphoproteins involved in lipid metabolism (ACACA, ACACB, PRKAB2, and PRKAG2, adjusted p value = 0.00027) were altered in pre-disease conditions. Alterations in phosphoproteins involved in regulation of fatty acid oxidation/synthesis (ACACB, PRKAB2, and PRKAG2, adjusted p value = 0.037), lipid homeostasis (9 proteins, adjusted p value = 0.0012), and lipid metabolism (15 proteins, p value = 3.36E-11) were observed in *Mat1a*$^{-/-}$ NASH. Taken together, *Mat1a* deficiency had an overall effect of lowering fatty acid oxidation and enhancing fatty acid synthesis (Table S3).

To understand the effect of how low cellular methylation capacity in *Mat1a*$^{-/-}$ changes the proteome, we next examined the proteomic changes after SAMe administration at different disease stages.

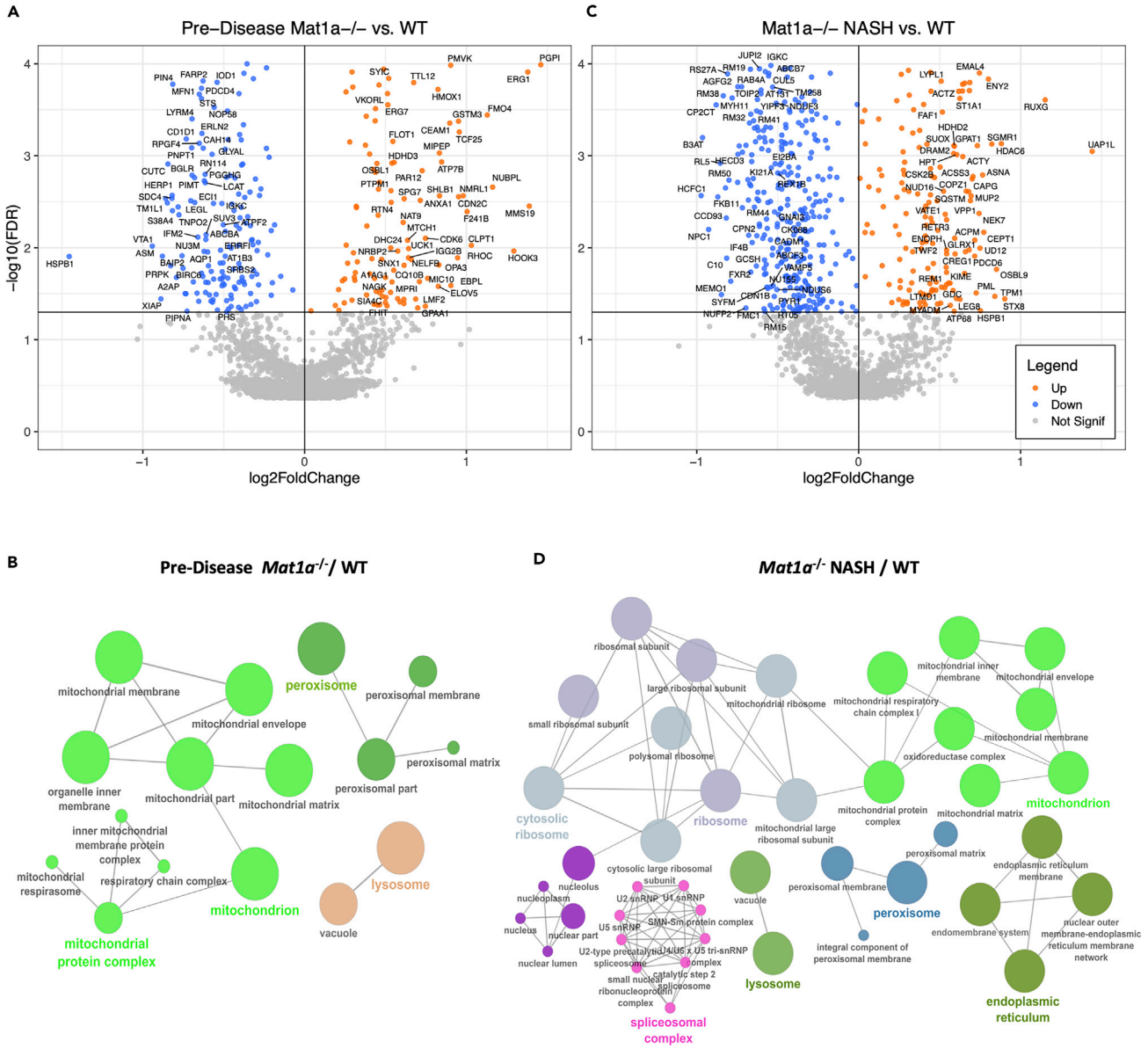

Figure 2. Proteomic changes in *Mat1a*$^{-/-}$ livers

(A) 411 proteins (FDR <1% and a fold change greater than 25% in either direction) were found in pre-disease *Mat1a*$^{-/-}$ animals compared to WT littermates aged four months (n = 4/condition). Of these proteins, 166 are increased in *Mat1a*$^{-/-}$ while 245 are decreased.

(B) ClueGO Ontology Analysis via PINE[19] for visualization of altered KEGG Cellular Components in pre-disease *Mat1a*$^{-/-}$ animals compared to WT littermates aged four months. Size of node denotes p value of enrichment.

(C) 921 proteins were found in *Mat1a*$^{-/-}$ animals aged ten months with NASH compared to WT littermates (n = 6/condition). Of these proteins, 294 are increased in *Mat1a*$^{-/-}$ while 627 are decreased.

(D) ClueGO Ontology Analysis via PINE for visualization of altered KEGG Cellular Components in *Mat1a*$^{-/-}$ animals aged ten months with NASH compared to WT littermates. Size of node denotes p value of enrichment.

Administration of SAMe to the pre-disease animals resulted in substantial (65%) reversal of phosphorylation with (112/172) phosphopeptides decreased with SAMe treatment (Figure 3A, Table 1). In *Mat1a*$^{-/-}$ NASH, there was an even stronger reversal (90%) in hyperphosphorylation signature of phosphorylated peptides (1081 of the 1109 sites) decreased with SAMe treatment (Figure 3D and Table 1). These phosphorylation changes were normalized to the total protein quantity in pre-disease *Mat1a*$^{-/-}$ and *Mat1a*$^{-/-}$ NASH (Table 1). The reversal in phosphorylation by SAMe treatment is widespread which suggests that there is global deactivation of kinases and/or activation of phosphatases. Specifically, enrichment in established

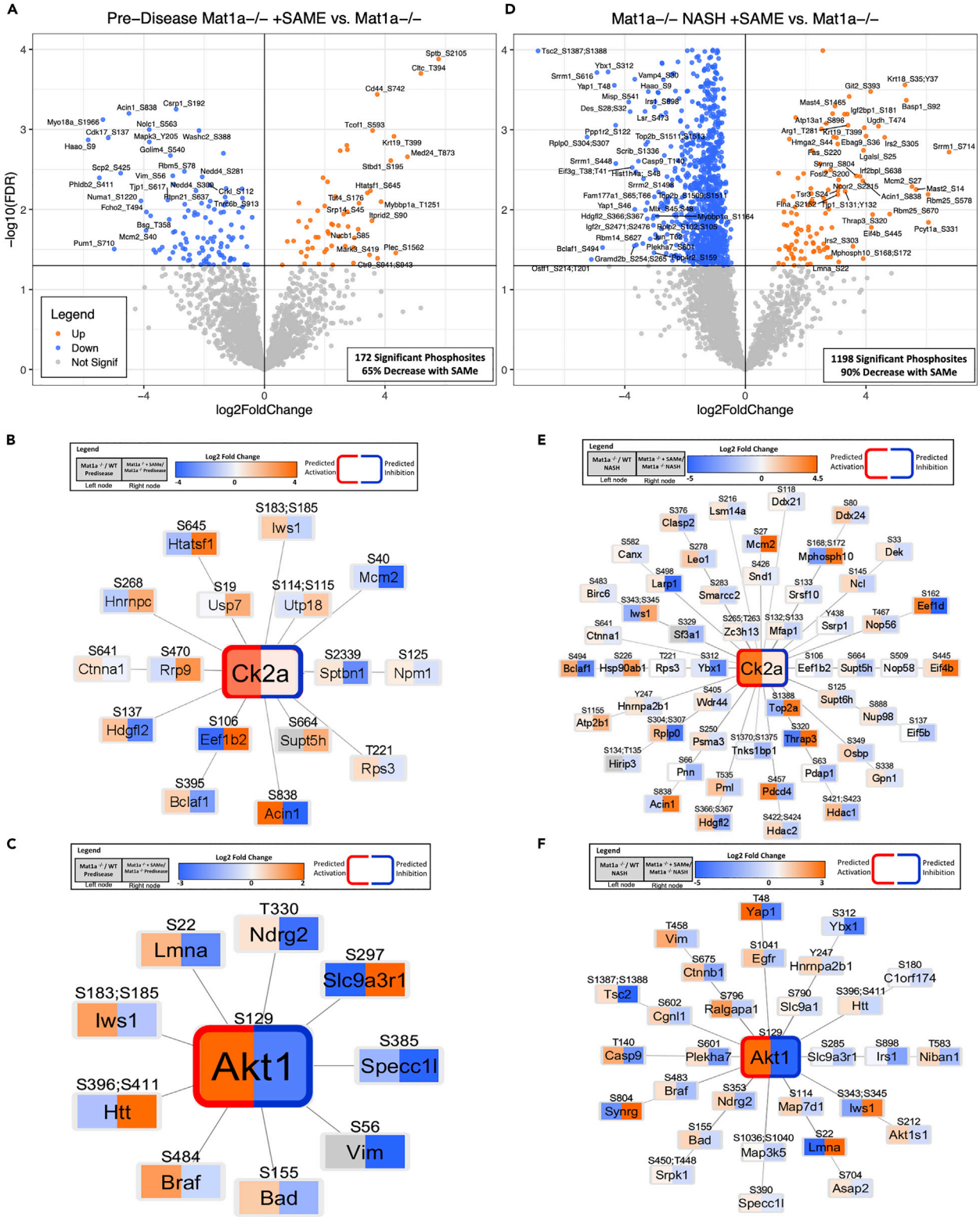
A
Pre–Disease Mat1a–/– +SAME vs. Mat1a–/–
−log10(FDR)
log2FoldChange
Legend
Up
Down
Not Signif
172 Significant Phosphosites
65% Decrease with SAMe
D
Mat1a–/– NASH +SAME vs. Mat1a–/–
1198 Significant Phosphosites
90% Decrease with SAMe
B
Ck2a
Iws1
Htatsf1
Mcm2
Usp7
Utp18
Hnrnpc
Ctnna1
Rrp9
Sptbn1
Npm1
Hdgfl2
Eef1b2
Supt5h
Rps3
Bclaf1
Acin1
E
Ck2a
C
Akt1
Lmna
Ndrg2
Slc9a3r1
Iws1
Specc1l
Htt
Vim
Braf
Bad
F
Akt1
Yap1
Ybx1
Vim
Egfr
Hnrnpa2b1
Ctnnb1
Tsc2
Ralgapa1
Slc9a1
Htt
Casp9
Plekha7
Slc9a3r1
Irs1
Niban1
Braf
Ndrg2
Map7d1
Iws1
Synrg
Bad
Map3k5
Lmna
Akt1s1
Srpk1
Asap2
Specc1l

Figure 3. Phospho-proteomic changes with SAMe treatment in *Mat1a*$^{-/-}$ livers

(A) 172 phosphopeptides (FDR <1% and a fold change greater than 25% in either direction) were found in in pre-disease *Mat1a*$^{-/-}$ animals treated with 100 mg/kg of SAMe for seven days were compared to *Mat1a*$^{-/-}$ animals treated with PBS for seven days (n = 4/condition). Of these phosphopeptides, 60 are increased with SAMe treatment while 120 are decreased.

(B) Phosphorylation analysis shows downstream CK2α targets which are normalized with SAMe treatment in pre-disease *Mat1a*$^{-/-}$. The left node of the bicolor node represents the pre-disease condition, and the right node represents the pre-disease condition treated with SAMe. The color gradient of the bicolor nodes is the range of log2-fold changes from predicted inhibition (blue gradient) to activation (orange gradient).

(C) IPA phosphorylation analysis found AKT1 was predicted to be decreased with SAMe treatment and normalized in pre-disease *Mat1a*$^{-/-}$ (activation *Z* score = −1.57, adjusted p value = 5.36E-3). The bicolor nodes are defined as in "B" above.

(D) 1198 phosphopeptides (FDR <1% and a fold change greater than 25% in either direction) were found in in *Mat1a*$^{-/-}$ animals with NASH treated with 30 mg/kg of SAMe for five days a week for eight weeks as compared to *Mat1a*$^{-/-}$ animals treated with PBS (n = 5/condition). Of these proteins, 117 are increased with SAMe treatment in *Mat1a*$^{-/-}$ while 1081 are decreased.

(E) IPA phosphorylation analysis found CK2α was predicted to be inhibited and normalized with SAMe treatment in *Mat1a*$^{-/-}$ NASH (activation *Z* score = −4.715, adjusted p value = 6.89E-12). $^{-/-}$. The left node of the bicolor node represents the NASH condition, and the right node represents the NASH condition treated with SAMe. The color gradient of the bicolor nodes is the range of log2-fold changes from predicted inhibition (blue gradient) to activation (orange gradient).

(F) IPA phosphorylation analysis found AKT1 was predicted to be inhibited and normalized with SAMe treatment in *Mat1a*$^{-/-}$ NASH (activation *Z* score = −3.813, adjusted p value = 1.43E-2). The bicolor nodes are defined as in "E" above.

downstream phosphotargets of AKT1 shows activation in pre-disease *Mat1a*$^{-/-}$ livers that were normalized by treatment with SAMe (Figure 3C). There is also inhibition in CK2α phosphotargets, such as residue Ser641 of α-catenin in SAMe-treated pre-disease *Mat1a*$^{-/-}$ compared to pre-disease *Mat1a*$^{-/-}$ alone, consistent with an inhibition and normalization of CK2α (Figures 3B and S4). Furthermore, SAMe administration decreased (25%, p value = 0.012) phosphorylation of AKT1 at Ser^{129}, a known activating residue phosphorylated by CK2.[21–23] In *Mat1a*$^{-/-}$ NASH, ingenuity pathway analysis also predicted that SAMe treatment inhibits both AKT1 and CK2α and normalizes their downstream phosphotargets. Consistently, SAMe administration inhibited both CK2α protein levels (32% compared to WT control, 7.95E-8 FDR) (Figure 3E) and AKT1 Ser129 (51.7% compared to WT control, p value = 0.04) (Figure 3F). In pre-disease *Mat1a*$^{-/-}$ mice, SAMe treatment enhanced the levels of the phosphatase, CPPED, by 44% compared to *Mat1a*$^{-/-}$ KO (0.027 FDR) and normalized CPPED to WT levels. In NASH condition, SAMe treatment caused an 11.1% induction in CPPED compared to *Mat1a*$^{-/-}$ KO (0.289 FDR) and normalized CPPED to WT levels. In *Mat1a*$^{-/-}$ NASH, SAMe administration also raised PPP5C level by 25% (FDR = 0.12) (Table S4). Additionally, based exclusively on our phosphoproteomics analysis, activation was predicted for PPP1CA (activation *Z* score = −2.425, adjusted p value = 5.99E-3) and PTPN11 (activation *Z* score = −2.456, adjusted p value = 2.26E-2) with SAMe administration in *Mat1a*$^{-/-}$ NASH (Figure S5).

To better understand the impact of SAMe administration on the total proteome (Table 1) in the pre-disease (134 proteins, Figure 4A) and in the *Mat1a*$^{-/-}$ NASH mode (379 proteins, Figure 4C), we focused on the SAMe-sensitive differentially expressed proteins. In pre-disease animals, peroxisomal proteins dominated, with 26/29 (89%) decreased with SAMe administration (adjusted p value 4.25E-47, Figure 4B). This also occurred in *Mat1a*$^{-/-}$ NASH but in addition to peroxisomal proteins there were SAMe-sensitive enrichment in proteins belonging to the mitochondria, ribosome, and ER subproteomes (Figures 4D and S6) and a decrease in mitochondrial β-oxidation components that were normalized by SAMe treatment (Figure S6).

Next, we determined whether there was conservation of the disease signature between *Mat1a*$^{-/-}$ NASH model and human NAFLD and found synergy with widespread hyperphosphorylation of the proteome and protein abundance changes in the mitochondria and the peroxisome subproteomes. Based on phosphoproteomics analysis of 13 liver biopsies from patients with NAFLD with various levels of steatosis and fibrosis (see Table 2 for clinical characterization), there were two major clusters and although they did not correlate with the degree of steatosis or fibrosis (Figures 5A and 5B), one cluster was similar to *Mat1a*$^{-/-}$ mice with respect to the phosphoprotein signature. Thus, we denoted the group that is similar to *Mat1a*$^{-/-}$ mice M-subtype (n = 10) and the other group non-M subtype (n = 3). Seven of the 10 M-subtype patients were confirmed to have serum metabolomic and lipidomic signature that resemble *Mat1a*$^{-/-}$ NASH.[8] As found with the *Mat1a*$^{-/-}$ NASH model, there was a global hyperphosphorylation signature (normalized to total protein levels) in the M-subtype versus non-M human NAFLD, with 71% (649/914) phosphopeptides higher in the M-subtype group. Intriguingly, CK2α was predicted to be activated in the M-subtype (activation *Z* score 4.382, adjusted p value 1.08E-14) and the CK2α target, phospho-S641-α-catenin, exhibited a 2-fold induction (FDR = 0.167) (Figure 5C), similar to the observed CK2α activation in both pre-disease and *Mat1a*$^{-/-}$ NASH (Figure 5D). These samples also show predicted activation of AKT1, like pre-disease

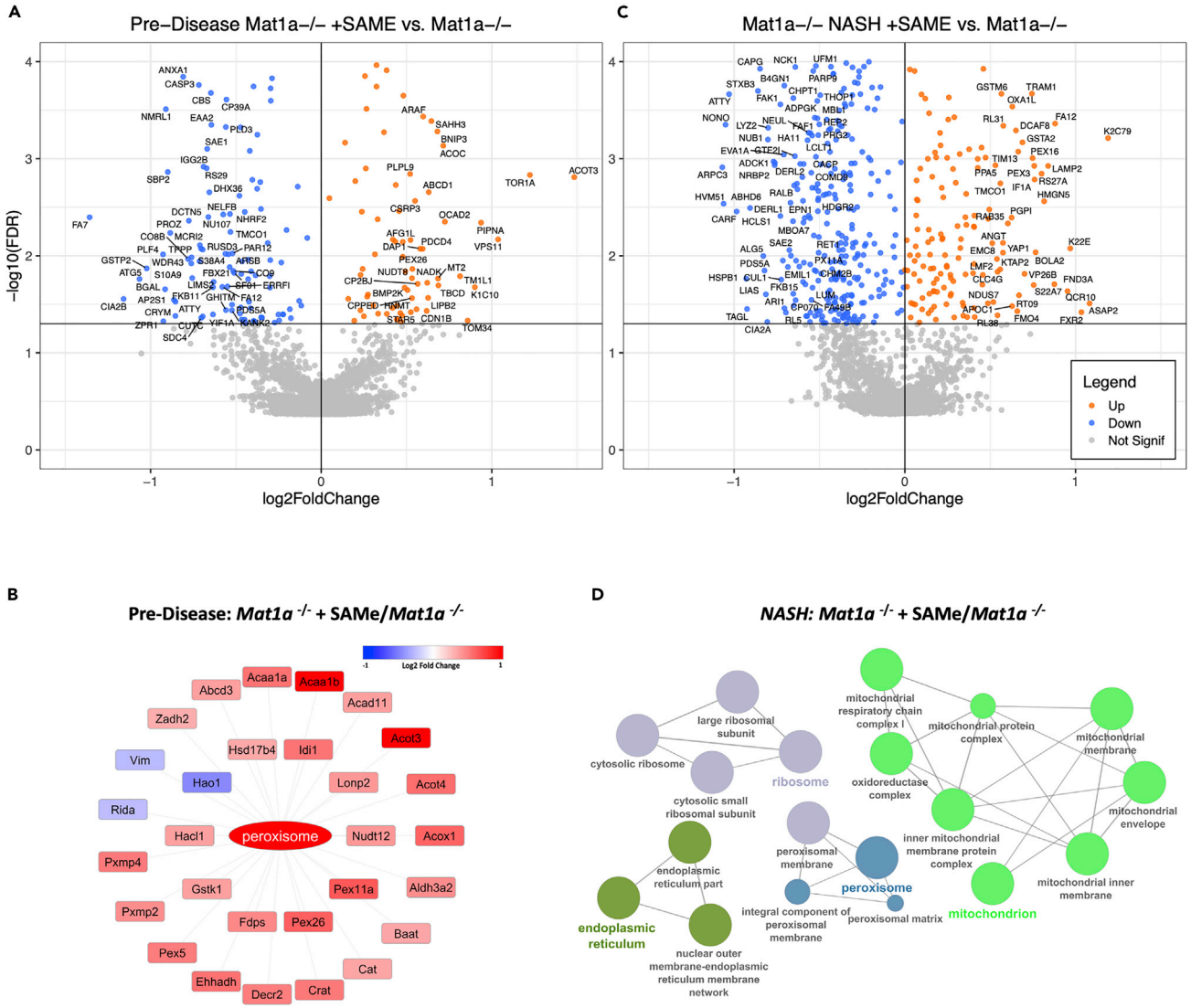

Figure 4. Proteomic changes with SAMe administration in *Mat1a*$^{-/-}$ livers

(A) 134 proteins (FDR <1% and a fold change greater than 25% in either direction) were found in pre-disease *Mat1a*$^{-/-}$ animals treated with 100 mg/kg of SAMe for seven days as compared to *Mat1a*$^{-/-}$ animals treated with PBS for seven days (n = 4/condition). Of these proteins, 71 are increased with SAMe administration while 63 are decreased with the addition of SAMe.

(B) Upstream regulator analysis using IPA found a strong predicted activation of PPARA with SAMe administration to pre-disease *Mat1a*$^{-/-}$ (*Z* score = 3.379, p value = 1.08E-27) which normalizes PPARA.

(C) Cystoscope visualization of proteins from the most enriched KEGG Cellular Components in pre-disease *Mat1a*$^{-/-}$ treated with SAMe vs *Mat1a*$^{-/-}$ generated using PINE.[19] Fold changes of proteins are represented as colors from blue to red.

(D) ClueGO Ontology Analysis via PINE for visualization of altered KEGG Cellular Components in *Mat1a*$^{-/-}$ animals aged ten months with NASH treated with SAMe compared to animals treated with PBS. Size of node denotes p value of enrichment.

Mat1a$^{-/-}$ animals (Figure 5D). Furthermore, there was an enrichment in differentially expressed mitochondrial, ribosomal, spliceosomal, and proteasomal proteins in M-subtype NAFLD when compared to non-M NAFLD (Figure 6B). These altered organelles have significant overlap with *Mat1a*$^{-/-}$ NASH and suggest a similar pathophysiology in *Mat1a*$^{-/-}$ NASH and human M-subtype NAFLD.

Similar to *Mat1a*$^{-/-}$ livers, there was a subset of dysregulated serine and threonine and dual-specificity phosphatases that show decreased expression in M-subtype compared to non-M subtype NAFLD (8/12). These include DUSP23, PP5C, and PTPA that were unique to human and PPM1F that was similar to the

Table 2. Subtyping human NASH

Sample Information		NASH Stages				Clinical Characteristics				Subtyping Results	
Sample ID	Collection Date	F0	F1	F2	F3	Steatosis	Lobular inflammation	Hepatocyte Ballooning	Fibrosis	Metabolomics Subtype	Phospho-Proteomics Subtype
NAFLD9	5/2/2019			X		~25%	not identified	not identified	2	Type M	Type M
NAFLD11	12/12/2017		X			25%	not identified	not identified	1a	Type M	Type M
NAFLD13	3/26/2018		X			10%	scant	not identified	1a	Type M	Type M
NAFLD2	3/26/2018		X			30%	not identified	not identified	1a	Type M	Type M
NAFLD10	5/3/2018		X			10%–15%	mild, lymphoid, focal	not identified	1a	Type M	Type M
NAFLD3	12/29/2017			X		<10%	mild	not identified	2	Type M	Type M
NAFLD7	5/22/2018				X	40%	scant	not identified	3	Type M	Type M
NAFLD1	10/13/2017		X			20%–30%	not identified	not identified	1a		Type M
NAFLD8	2/27/2018		X			40%	not identified	not identified	1a		Type M
NAFLD12	10/31/2019		X			10%–20%	Few ceroid macrophages	not identified	1a		Type M
NAFLD6	8/28/2018		X			30%	not identified	rare	1a		Non-M
NAFLD4	7/26/2019		X			60%	not identified	not identified	1a		Non-M
NAFLD5	2/2/2018		X			50%	patchy glycogenic nuclei	not identified	1a		Non-M

animal model (Table S5). Taken together, M-subtype human NAFLD also have lower expression of multiple phosphatases and they may contribute to the observed global hyperphosphorylation.

DISCUSSION

Analyzing the proteome and phosphoproteome at different stages of progression of the *Mat1a*$^{-/-}$ NASH model has provided insight into the temporal order of the cellular pathways associated with disease progression. Early pre-disease animals primarily exhibited alterations in the mitochondria, peroxisome, and lysosome subproteomes with specific induction in peroxisomal β-oxidation and a decrease in mitochondrial β-oxidation components. This may represent the stress on lipid metabolism machinery to metabolize excess lipids before visible steatosis (Table S3). Mitochondrial dysfunction in NASH is a well-known phenomenon[24,25] and our group has recently reported the role of MAT1A's influence on mitochondrial function.[26] In addition to the pathways altered in the pre-disease state, the NASH stage also exhibits dysregulation of ER proteins, cytosolic ribosomes, spliceosomes, and nuclear proteins that are associated with the onset of steatosis and subsequent inflammation and fibrosis and transition to hepatocellular carcinoma[27–29] (Table S3).

There is a global hyperphosphorylation signature at all stages of the *Mat1a*$^{-/-}$ NASH model which is consistent with CK2α activation. CK2α is the catalytic subunit of casein kinase 2 (CK2) that is a ubiquitously expressed, constitutively active.[30,31] CK2 is known to be involved in cell cycle progression[30] and is overexpressed in HCC.[32] CK2 regulates a multitude of pathways including AKT1,[21,33] NF-κB,[34] TGF-β,[35] ERK2, β-catenin, and WNT signaling.[15] CK2 activation has been reported in type 2 diabetes[36] and obesity where it was shown to regulate lipogenesis and triglyceride levels[37] and AKT1-mediated glucose metabolism and insulin signaling by direct phosphorylation of AKT1 Ser129 and indirectly through PTEN inhibition.[22,23,33,] CK2 was recently shown to be increased in patients with NAFLD, with its expression correlating to disease severity.[38] Importantly, we found in pre-disease and *Mat1a*$^{-/-}$ NASH CK2α and AKT1 activation. Previous reports have shown that AKT1 activation in a SAMe-deficient system is due to LKB1 and that *Mat1a*$^{-/-}$ animals have increased LKB1 activity.[14] We confirmed increased LKB1 (STK11 Ser31) phosphorylation in pre-disease *Mat1a*$^{-/-}$ animals but our current findings also implicate direct phosphorylation of AKT1 Ser129 by CK2 in the *Mat1a*$^{-/-}$ NASH model at all disease stages.

Through global phosphoproteomics, insights were gained on the broad effects of SAMe administration on the proteome in the *Mat1a*$^{-/-}$ NASH model. We observed a drastic reduction and normalization of

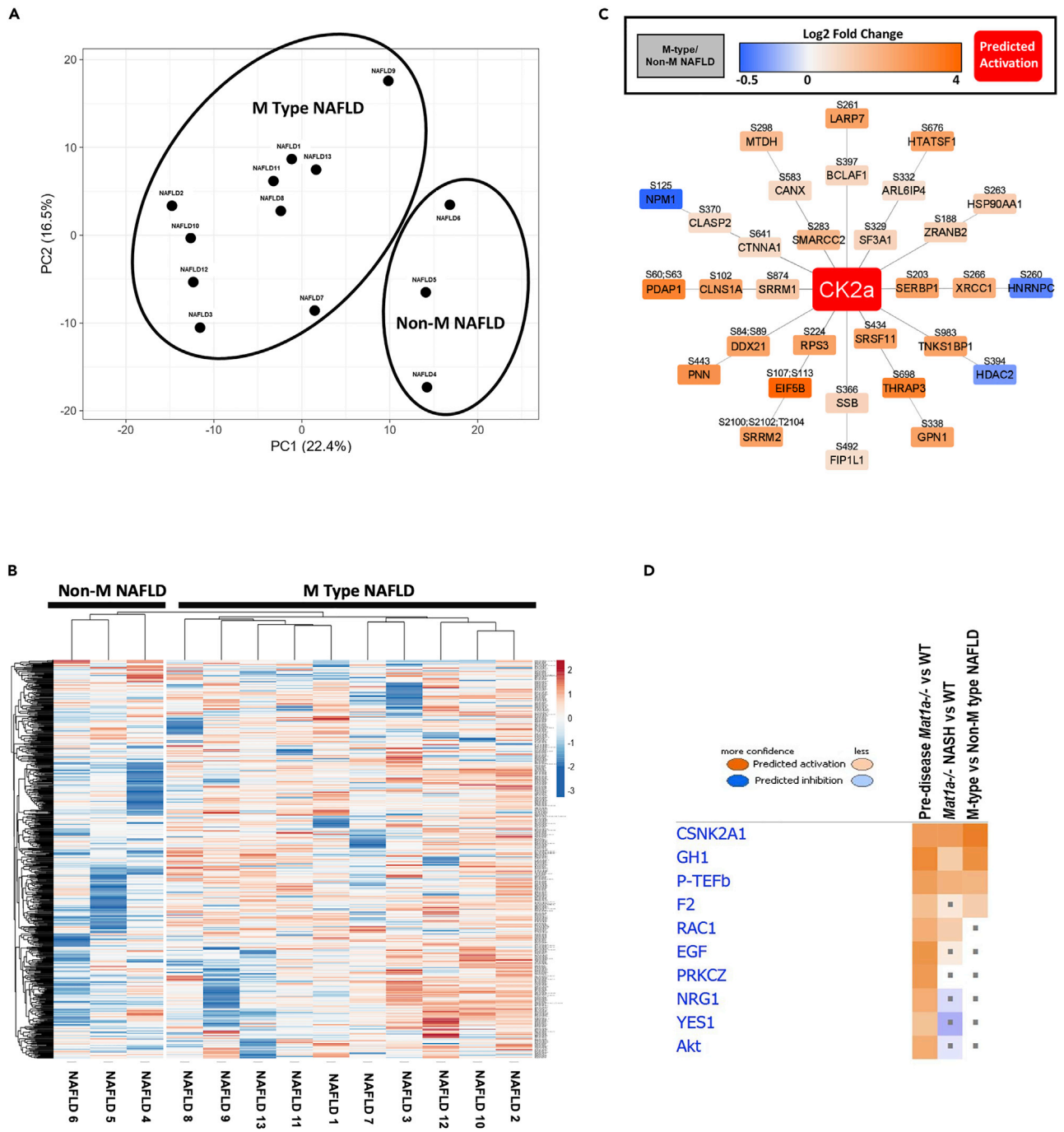

Figure 5. Phospho-proteomic changes in human NAFLD with comparisons to *Mat1a* $^{-/-}$ KO model

(A) Principal component analysis of phosphoproteomic changes acquisitions from human NASH. Original values are ln(x)-transformed. Unit variance scaling is applied to rows; SVD with imputation is used to calculate principal components.

(B) Heatmap of human phosphoproteomics data. Rows were centered and phosphopeptide intensities were log transformed; unit variance scaling is applied to rows. Both rows and columns are clustered using Manhattan distance and average linkage.

(C) IPA phosphorylation analysis found CK2α predicted to be activated in the M-subtype NASH when compared to non-M subtype NASH (activation *Z* score 4.382, adjusted p value 1.08E-14) (activation *Z* score = 2.83, adjusted p value = 1.06E-3).

(D) IPA phosphoproteomic upstream regulator analysis comparing activation status of predicted upstream regulators in pre-disease *Mat1a* $^{-/-}$ animals, *Mat1a* $^{-/-}$ animals with NASH, and human M-subtype NASH.

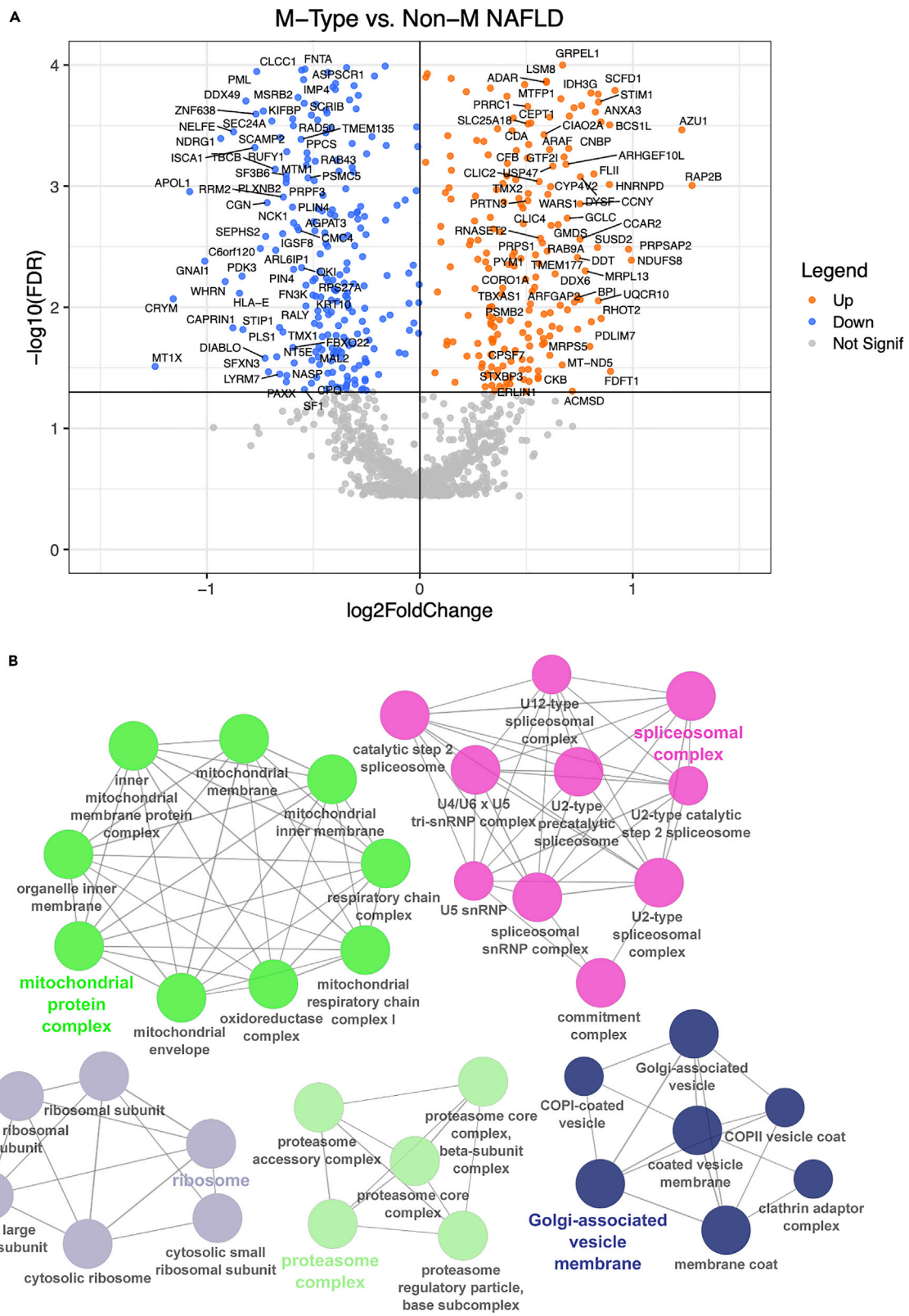
A
M−Type vs. Non−M NAFLD
−log10(FDR)
log2FoldChange
Legend
Up
Down
Not Signif
B
inner mitochondrial membrane protein complex
mitochondrial membrane
mitochondrial inner membrane
organelle inner membrane
respiratory chain complex
mitochondrial protein complex
mitochondrial envelope
oxidoreductase complex
mitochondrial respiratory chain complex I
catalytic step 2 spliceosome
U12-type spliceosomal complex
spliceosomal complex
U4/U6 x U5 tri-snRNP complex
U2-type precatalytic spliceosome
U2-type catalytic step 2 spliceosome
U5 snRNP
spliceosomal snRNP complex
U2-type spliceosomal complex
commitment complex
ribosomal subunit
large ribosomal subunit
ribosome
cytosolic large ribosomal subunit
cytosolic ribosome
cytosolic small ribosomal subunit
proteasome accessory complex
proteasome core complex, beta-subunit complex
proteasome core complex
proteasome complex
proteasome regulatory particle, base subcomplex
Golgi-associated vesicle
COPI-coated vesicle
COPII vesicle coat
coated vesicle membrane
Golgi-associated vesicle membrane
clathrin adaptor complex
membrane coat

Figure 6. Proteomic changes in human NAFLD

(A) 974 proteins (FDR <1% and a fold change greater than 25% in either direction) were found in M-subtype NAFLD when compared to non-M subtype NAFLD (M-subtype NAFLD, n = 10, Non-M subtype, n = 3). Of these proteins, 424 are increased in M-subtype NAFLD while 550 are decreased in M-subtype NAFLD.

(B) ClueGO Ontology Analysis via PINE[19] for visualization of altered KEGG Cellular Components in human M-subtype NAFLD vs non-M subtype NAFLD. Size of node denotes p value of enrichment.

the phosphoproteome with 90% of the differentially expressed phosphopeptides decreased with SAMe administration in *Mat1a*$^{-/-}$ NASH (Figure 3C). This phosphorylation signature is representative, at least in part, of CK2α and AKT1 normalization (Figure 3). *Mat1a*$^{-/-}$ mice are known to have higher β-catenin activity and SAMe administration was shown to inhibit β-catenin activation in liver and colon cancer cells[39] but the underlying mechanism was unclear. SAMe administration also normalized hyperactive ERK2 in the *Mat1a*$^{-/-}$ livers[12] and reversed disease progression in *Mat1a*$^{-/-}$ NASH.[8] CK2 regulates β-catenin through WNT-dependent and independent signaling. One mode of control of β-catenin is via its interaction with α-catenin that is known to inhibit β-catenin's transcriptional activity in cancer cells.[15] Growth factor-mediated ERK activation enhances CK2 activity that in turn phosphorylates α-catenin at Ser641 residue,[15] which inhibits α-catenin's interaction with β-catenin leading to activation of β-catenin transcriptional activity. SAMe administration reversed hyperphosphorylation of Ser641-α-catenin in both *Mat1a*$^{-/-}$ pre-disease and NASH, suggesting this may be a key mechanism for SAMe to inhibit β-catenin signaling in this model. Importantly, we also found Ser641-α-catenin hyperphosphorylation in human M-subtype NAFLD versus non-*M*-subtype NAFLD. Augmented β-catenin-dependent transcription is also dependent on phosphorylation of AKT at Ser129 by CK2.[22] CK2α-enhancing effects on β-catenin transcriptional activity are reversed when an AKT mutant deficient in Ser129 phosphorylation by CK2 is co-expressed.[22] Our data showing AKT1 Ser^{129} phosphorylation induced in *Mat1a*$^{-/-}$ pre-disease and NASH and normalized by SAMe support the activation of CK2-β-catenin pathway can be normalized by SAMe treatment (Figures 1C and 1D).

Regulation of CK2 signaling is not fully elucidated, as it is constitutively active[31] and not regulated like a traditional kinase through phosphorylation of its activation loop.[40,41] In fact, recent studies have shown that modulation of CK2 activity is dependent on post-translational modifications (PTMs), and CK2-mediated phosphorylation requires precise positioning of multiple adjacent phosphorylated residues or other PTM-modified sites including methylation, acetylation, or sumoylation.[42,43] Our previous work has shown that the *Mat1a*$^{-/-}$ NASH model has decreased acetyl-CoA and accompanying protein acetylation, as well as decreased SAMe and subsequent DNA and protein methylation.[8,44] In addition, SUMOylation is controlled by SAMe levels and that the *Mat1a*$^{-/-}$ NASH model has increased SUMOylated RanGAP1 which is normalized by SAMe administration.[45] The proposition that the combinatorial nature of dysregulated PTMs in the *Mat1a*$^{-/-}$ NASH might result in CK2 activation is intriguing but more work needs to be done to determine the role of each dysregulated PTM.

Global hyperphosphorylation does not occur often in biology, as phosphorylation is a tightly controlled mechanism for cellular signal transduction and is regulated by the availability of ATP, kinase activity, and levels of protein phosphatases[46,47] and suggests a coordinated multiprong signaling. *Mat1a*$^{-/-}$ animals have higher activity of multiple kinases, such as ERK, LKB1, AKT, and AMPK[12–14] and lower activity of the phosphatase DUSP1.[12] In our study, increased phosphorylation in pre-disease *Mat1a*$^{-/-}$ may partially be attributed to decreased protein phosphatases (Table S1) such as SHOC2, a regulatory subunit of PP1C, which has recently been implicated to regulate RAF-ERK via its phosphatase activity.[48]

Mat1a$^{-/-}$ NASH livers also have decreased protein phosphatases including serine/threonine-protein phosphatase CPPED1, which is known to dephosphorylate AKT1 Ser473.[16] This could potentially contribute to increased AKT activity along with the CK2α-mediated activation of AKT through Ser^{129} phosphorylation. It is challenging to pinpoint the root cause of global hyperphosphorylation in the *Mat1a*$^{-/-}$ NASH model, as along with decreased protein phosphatases (Tables S1 and S2), global SAMe and acetyl-CoA levels are decreased causing subsequent decreases in global protein methylation and acetylation plus increased protein SUMOylation.[8,44,45] SAMe administration in the *Mat1a*$^{-/-}$ NASH model normalizes protein phosphatases (Table S4) as well as SAMe levels and SUMOylation.[8,44] More work needs to be done to understand the temporal order of the different PTMs in the *Mat1a*$^{-/-}$ NASH model to better understand how SAMe depletion results in these changes.

Comparison of serum metabolomics from *Mat1a*$^{-/-}$ mice with NASH to human patients with NAFLD revealed nearly 50% of patients with NAFLD have a very similar profile as *Mat1a*$^{-/-}$ mice, which we termed M-subtype.[8] However, the molecular underpinnings of this subtype of human NASH have yet to be determined. By studying the phosphoproteome from liver biopsies of patients with M-subtype NAFLD, we have for the first time determined that not only do the serum lipids and metabolites of these patients resemble *Mat1a*$^{-/-}$ serum[8] but they also share the liver hyperphosphorylation signature highlighted by CK2α activation which is independent of the degree of steatosis and fibrosis (Figure 5C and Table 1). Taken together with CK2-mediated activation of AKT1 in the *Mat1a*$^{-/-}$ NASH model at all disease stages, we now have a better understanding of the etiology of a major subtype of human NAFLD and further the relevancy of the *Mat1a*$^{-/-}$ NASH model to accurately recapitulate a major subtype of human disease.

Like the *Mat1a*$^{-/-}$ NASH model, M-subtype human NAFLD livers have decreased phosphatase activity when compared to non-M subtype NAFLD (Table S5). The decrease in PPP5C is particularly interesting because PPP5C is known to regulate ERK2,[49] a kinase we have reported to be activated in *Mat1a*$^{-/-}$ NASH and to be SAMe responsive.[12] In addition, PPP5C has also been reported to act as a physiological inhibitor of ASK1 through its phosphatase activity.[17] Strategies to inhibit ASK1 to treat NASH have shown great pre-clinical promise.[50,51] However, recent phase 3 clinical trials using selonsertib, an ASK1 inhibitor, were not able to suppress fibrosis.[52,53] Inclusion criteria for these trials did not include serum lipidomic and metabolic subtyping. Based on the results from this study and the ability to subtype human NAFLD via serum,[8] we speculate that selonsertib may have greater success on M-subtype than non-M subtype NAFLD.

The results from this study also implore further research to be carried out using SAMe as a treatment in human M-subtype NAFLD. To date, SAMe administration in human liver disease has had mixed results but has shown benefit in intrahepatic cholestasis and a near-significant benefit in alcoholic liver disease.[54] With the ability to accurately subtype human disease via non-invasive serum metabolomic and lipidomic measurements,[8] the use of SAMe in the patients with M-subtype NAFLD warrants further study.

In conclusion, this study has uncovered in the *Mat1a*$^{-/-}$ model disease phophoproteome signatures occurring prior to any observable pathological phenotype and that this hyperphosphorylation signature is expanded with *Mat1a*$^{-/-}$ NASH that was dramatically reversed with SAMe treatment. This hyperphosphorylation signature is also observed in humans with M-subtype NAFLD, which may have pathophysiological and therapeutic implications.

Limitations of the study

Our study provides a comprehensive characterization of the phosphoproteome of the liver during the development and progression of NAFLD in the setting of chronically low hepatic SAMe level. Activation of AKT and CK2 was seen in both murine model and in humans with NAFLD that share the same metabolomic signature. However, this is an association and the causal role of these kinases in the development and progression of NAFLD remains to be examined. In addition, although we identified pathways that were normalized by SAMe administration, the underlying molecular mechanisms of SAMe's actions remain unclear.

STAR★METHODS

Detailed methods are provided in the online version of this paper and include the following:

- KEY RESOURCES TABLE
- RESOURCE AVAILABILITY
  - Lead contact
  - Materials availability
  - Data and code availability
- EXPERIMENTAL MODEL AND SUBJECT DETAILS
  - Animals
  - Human tissues
- METHOD DETAILS
  - Sample preparation for proteomic analysis
  - Titanium dioxide phospho enrichment
  - Quantitation of individual specimen by DIA-MS

- DIA-MS data normalization, quantitation, and visualization
- Phospho enrichment database searches and quantification
- Triglyceride measurement
- ALT/AST assay
- H&E staining
- Hepatic peroxisome and mitochondria staining

- QUANTIFICATION AND STATISTICAL ANALYSIS

SUPPLEMENTAL INFORMATION

Supplemental information can be found online at https://doi.org/10.1016/j.isci.2023.105987.

ACKNOWLEDGMENTS

This work was supported by US National Institutes of Health (NIH) Grant R01DK123763 (S.C.L., K.R., J.M.M., and J.E.V.E.), Agencia Estatal de Investigación, Spain Grants MINECO SAF 2017-88041-R, ISCiii PIE14/00031 CIBERehd-ISCiii, and Severo Ochoa Excellence Accreditation SEV-2016-0644 (J.M.M.) and the Cedars-Sinai Proteomic and Metabolomic Core Facility.

AUTHOR CONTRIBUTIONS

The manuscript was written through contributions of all authors. All authors have given approval to the final version of the manuscript.

DECLARATION OF INTERESTS

M.N.s has been on the advisory board for 89BIO, Gilead, Intercept, Pfizer, Novartis, Novo Nordisk, Allergan, Blade, EchoSens, Fractyl, Terns, OWL, Siemens, Roche diagnostic, and Abbott; M.N. has received research support from Allergan, BMS, Gilead, Galmed, Galectin, Genfit, Conatus, Enanta, Madrigal, Novartis, Shire, Viking, and Zydus; M.N. is a minor shareholder or has stocks in Anaetos and Viking. J.M.M. is on the scientific advisory board of OWL Metabolomics.

Received: May 16, 2022
Revised: September 15, 2022
Accepted: January 11, 2023
Published: February 17, 2023

REFERENCES

1. Younossi, Z.M., Koenig, A.B., Abdelatif, D., Fazel, Y., Henry, L., and Wymer, M. (2016). Global epidemiology of nonalcoholic fatty liver disease-Meta-analytic assessment of prevalence, incidence, and outcomes. Hepatology *64*, 73–84.

2. Cohen, J.C., Horton, J.D., and Hobbs, H.H. (2011). Human fatty liver disease: old questions and new insights. Science *332*, 1519–1523.

3. Diehl, A.M., and Day, C. (2017). Cause, pathogenesis, and treatment of nonalcoholic steatohepatitis. N. Engl. J. Med. *377*, 2063–2072.

4. Anstee, Q.M., Targher, G., and Day, C.P. (2013). Progression of NAFLD to diabetes mellitus, cardiovascular disease or cirrhosis. Nat. Rev. Gastroenterol. Hepatol. *10*, 330–344.

5. Noureddin, M., Vipani, A., Bresee, C., Todo, T., Kim, I.K., Alkhouri, N., Setiawan, V.W., Tran, T., Ayoub, W.S., Lu, S.C., et al. (2018). NASH leading cause of liver transplant in women: updated analysis of indications for liver transplant and ethnic and gender variances. Am. J. Gastroenterol. *113*, 1649–1659.

6. Farrell, G., Schattenberg, J.M., Leclercq, I., Yeh, M.M., Goldin, R., Teoh, N., and Schuppan, D. (2019). Mouse models of nonalcoholic steatohepatitis: toward optimization of their relevance to human nonalcoholic steatohepatitis. Hepatology *69*, 2241–2257.

7. Hansen, H.H., Feigh, M., Veidal, S.S., Rigbolt, K.T., Vrang, N., and Fosgerau, K. (2017). Mouse models of nonalcoholic steatohepatitis in preclinical drug development. Drug Discov. Today *22*, 1707–1718.

8. Alonso, C., Fernández-Ramos, D., Varela-Rey, M., Martínez-Arranz, I., Navasa, N., Van Liempd, S.M., Lavín Trueba, J.L., Mayo, R., Ilisso, C.P., de Juan, V.G., et al. (2017). Metabolomic identification of subtypes of nonalcoholic steatohepatitis. Gastroenterology *152*, 1449–1461.e7.

9. Lu, S.C., Alvarez, L., Huang, Z.Z., Chen, L., An, W., Corrales, F.J., Avila, M.A., Kanel, G., and Mato, J.M. (2001). Methionine adenosyltransferase 1A knockout mice are predisposed to liver injury and exhibit increased expression of genes involved in proliferation. Proc. Natl. Acad. Sci. USA *98*, 5560–5565.

10. Chiang, P.K., Gordon, R.K., Tal, J., Zeng, G.C., Doctor, B.P., Pardhasaradhi, K., and McCann, P.P. (1996). S-Adenosylmethionine and methylation. Faseb. J. *10*, 471–480.

11. Lu, S.C., and Mato, J.M. (2012). S-adenosylmethionine in liver health, injury, and cancer. Physiol. Rev. *92*, 1515–1542.

12. Tomasi, M.L., Ramani, K., Lopitz-Otsoa, F., Rodríguez, M.S., Li, T.W.H., Ko, K., Yang, H., Bardag-Gorce, F., Iglesias-Ara, A., Feo, F., et al. (2010). S-adenosylmethionine regulates dual-specificity mitogen-activated protein kinase phosphatase expression in mouse and human hepatocytes. Hepatology *51*, 2152–2161.

13. Vázquez-Chantada, M., Ariz, U., Varela-Rey, M., Embade, N., Martínez-Lopez, N., Fernández-Ramos, D., Gómez-Santos, L., Lamas, S., Lu, S.C., Martínez-Chantar, M.L., and Mato, J.M. (2009). Evidence for

LKB1/AMP-activated protein kinase/endothelial nitric oxide synthase cascade regulated by hepatocyte growth factor, S-adenosylmethionine, and nitric oxide in hepatocyte proliferation. Hepatology *49*, 608–617.

14. Martínez-López, N., Varela-Rey, M., Fernández-Ramos, D., Woodhoo, A., Vázquez-Chantada, M., Embade, N., Espinosa-Hevia, L., Bustamante, F.J., Parada, L.A., Rodriguez, M.S., et al. (2010). Activation of LKB1-Akt pathway independent of phosphoinositide 3-kinase plays a critical role in the proliferation of hepatocellular carcinoma from nonalcoholic steatohepatitis. Hepatology *52*, 1621–1631.

15. Ji, H., Wang, J., Nika, H., Hawke, D., Keezer, S., Ge, Q., Fang, B., Fang, X., Fang, D., Litchfield, D.W., et al. (2009). EGF-induced ERK activation promotes CK2-mediated disassociation of alpha-Catenin from beta-Catenin and transactivation of beta-Catenin. Mol. Cell *36*, 547–559.

16. Zhuo, D.X., Zhang, X.W., Jin, B., Zhang, Z., Xie, B.S., Wu, C.L., Gong, K., and Mao, Z.B. (2013). CSTP1, a novel protein phosphatase, blocks cell cycle, promotes cell apoptosis, and suppresses tumor growth of bladder cancer by directly dephosphorylating Akt at Ser473 site. PLoS One *8*, e65679.

17. Morita, K., Saitoh, M., Tobiume, K., Matsuura, H., Enomoto, S., Nishitoh, H., and Ichijo, H. (2001). Negative feedback regulation of ASK1 by protein phosphatase 5 (PP5) in response to oxidative stress. EMBO J. *20*, 6028–6036.

18. Ramani, K., Robinson, A.E., Berlind, J., Fan, W., Abeynayake, A., Binek, A., Barbier-Torres, L., Noureddin, M., Nissen, N.N., Yildirim, Z., et al. (2022). S-adenosylmethionine inhibits la ribonucleoprotein domain family member 1 in murine liver and human liver cancer cells. Hepatology *75*, 280–296.

19. Sundararaman, N., Go, J., Robinson, A.E., Mato, J.M., Lu, S.C., Van Eyk, J.E., and Venkatraman, V. (2020). PINE: an automation tool to extract and visualize protein-centric functional networks. J. Am. Soc. Mass Spectrom. *31*, 1410–1421.

20. Gould, S.J., and Collins, C.S. (2002). Opinion: peroxisomal-protein import: is it really that complex? Nat. Rev. Mol. Cell Biol. *3*, 382–389.

21. Di Maira, G., Salvi, M., Arrigoni, G., Marin, O., Sarno, S., Brustolon, F., Pinna, L.A., and Ruzzene, M. (2005). Protein kinase CK2 phosphorylates and upregulates Akt/PKB. Cell Death Differ. *12*, 668–677.

22. Ponce, D.P., Yefi, R., Cabello, P., Maturana, J.L., Niechi, I., Silva, E., Galindo, M., Antonelli, M., Marcelain, K., Armisen, R., and Tapia, J.C. (2011). CK2 functionally interacts with AKT/PKB to promote the β-catenin-dependent expression of survivin and enhance cell survival. Mol. Cell. Biochem. *356*, 127–132.

23. Di Maira, G., Brustolon, F., Pinna, L.A., and Ruzzene, M. (2009). Dephosphorylation and inactivation of Akt/PKB is counteracted by protein kinase CK2 in HEK 293T cells. Cell. Mol. Life Sci. *66*, 3363–3373.

24. Fromenty, B., Robin, M.A., Igoudjil, A., Mansouri, A., and Pessayre, D. (2004). The ins and outs of mitochondrial dysfunction in NASH. Diabetes Metab. *30*, 121–138.

25. Léveillé, M., and Estall, J.L. (2019). Mitochondrial dysfunction in the transition from NASH to HCC. Metabolites *9*, 233.

26. Murray, B., Peng, H., Barbier-Torres, L., Robinson, A.E., Li, T.W.H., Fan, W., Tomasi, M.L., Gottlieb, R.A., Van Eyk, J., Lu, Z., et al. (2019). Methionine adenosyltransferase α1 is targeted to the mitochondrial matrix and interacts with cytochrome P450 2E1 to lower its expression. Hepatology *70*, 2018–2034.

27. Grise, F., Bidaud, A., and Moreau, V. (2009). Rho GTPases in hepatocellular carcinoma. Biochim. Biophys. Acta *1795*, 137–151.

28. Bastide, A., and David, A. (2018). The ribosome, (slow) beating heart of cancer (stem) cell. Oncogenesis *7*, 34.

29. Ramani, K., Mato, J.M., and Lu, S.C. (2011). Role of methionine adenosyltransferase genes in hepatocarcinogenesis. Cancers *3*, 1480–1497.

30. Homma, M.K., and Homma, Y. (2008). Cell cycle and activation of CK2. Mol. Cell. Biochem. *316*, 49–55.

31. Turowec, J.P., Duncan, J.S., French, A.C., Gyenis, L., St Denis, N.A., Vilk, G., and Litchfield, D.W. (2010). Protein kinase CK2 is a constitutively active enzyme that promotes cell survival: strategies to identify CK2 substrates and manipulate its activity in mammalian cells. Methods Enzymol. *484*, 471–493.

32. Zhang, H.X., Jiang, S.S., Zhang, X.F., Zhou, Z.Q., Pan, Q.Z., Chen, C.L., Zhao, J.J., Tang, Y., Xia, J.C., and Weng, D.S. (2015). Protein kinase CK2α catalytic subunit is overexpressed and serves as an unfavorable prognostic marker in primary hepatocellular carcinoma. Oncotarget *6*, 34800–34817.

33. Borgo, C., Milan, G., Favaretto, F., Stasi, F., Fabris, R., Salizzato, V., Cesaro, L., Belligoli, A., Sanna, M., Foletto, M., et al. (2017). CK2 modulates adipocyte insulin-signaling and is up-regulated in human obesity. Sci. Rep. *7*, 17569.

34. Dominguez, I., Sonenshein, G.E., and Seldin, D.C. (2009). Protein kinase CK2 in health and disease: CK2 and its role in Wnt and NF-kappaB signaling: linking development and cancer. Cell. Mol. Life Sci. *66*, 1850–1857.

35. Kim, S., Ham, S., Yang, K., and Kim, K. (2018). Protein kinase CK2 activation is required for transforming growth factor β-induced epithelial-mesenchymal transition. Mol. Oncol. *12*, 1811–1826.

36. Lan, Y.C., Wang, Y.H., Chen, H.H., Lo, S.F., Chen, S.Y., and Tsai, F.J. (2020). Effects of casein kinase 2 alpha 1 gene expression on mice liver susceptible to type 2 diabetes mellitus and obesity. Int. J. Med. Sci. *17*, 13–20.

37. Viscarra, J.A., Wang, Y., Hong, I.H., and Sul, H.S. (2017). Transcriptional activation of lipogenesis by insulin requires phosphorylation of MED17 by CK2. Sci. Signal. *10*, eaai8596.

38. Choi, S.E., Kwon, S., Seok, S., Xiao, Z., Lee, K.W., Kang, Y., Li, X., Shinoda, K., Kajimura, S., Kemper, B., and Kemper, J.K. (2017). Obesity-linked phosphorylation of SIRT1 by casein kinase 2 inhibits its nuclear localization and promotes fatty liver. Mol. Cell Biol. *37*, e00006-17.

39. Li, T.W.H., Peng, H., Yang, H., Kurniawidjaja, S., Panthaki, P., Zheng, Y., Mato, J.M., and Lu, S.C. (2015). S-Adenosylmethionine and methylthioadenosine inhibit β-catenin signaling by multiple mechanisms in liver and colon cancer. Mol. Pharmacol. *87*, 77–86.

40. Sarno, S., Ghisellini, P., and Pinna, L.A. (2002). Unique activation mechanism of protein kinase CK2. The N-terminal segment is essential for constitutive activity of the catalytic subunit but not of the holoenzyme. J. Biol. Chem. *277*, 22509–22514.

41. Olsen, B.B., Guerra, B., Niefind, K., and Issinger, O.G. (2010). Structural basis of the constitutive activity of protein kinase CK2. Methods Enzymol. *484*, 515–529.

42. St-Denis, N., Gabriel, M., Turowec, J.P., Gloor, G.B., Li, S.S.C., Gingras, A.C., and Litchfield, D.W. (2015). Systematic investigation of hierarchical phosphorylation by protein kinase CK2. J. Proteonomics *118*, 49–62.

43. Nuñez de Villavicencio-Diaz, T., Rabalski, A.J., and Litchfield, D.W. (2017). Protein kinase CK2: intricate relationships within regulatory cellular networks. Pharmaceuticals *10*, 27.

44. Robinson, A.E., Binek, A., Venkatraman, V., Searle, B.C., Holewinski, R.J., Rosenberger, G., Parker, S.J., Basisty, N., Xie, X., Lund, P.J., et al. (2020). Lysine and arginine protein post-translational modifications by enhanced DIA libraries: quantification in murine liver disease. J. Proteome Res. *19*, 4163–4178.

45. Tomasi, M.L., Tomasi, I., Ramani, K., Pascale, R.M., Xu, J., Giordano, P., Mato, J.M., and Lu, S.C. (2012). S-adenosyl methionine regulates ubiquitin-conjugating enzyme 9 protein expression and sumoylation in murine liver and human cancers. Hepatology *56*, 982–993.

46. Ardito, F., Giuliani, M., Perrone, D., Troiano, G., and Lo Muzio, L. (2017). The crucial role of protein phosphorylation in cell signaling and its use as targeted therapy (Review). Int. J. Mol. Med. *40*, 271–280.

47. Ubersax, J.A., and Ferrell, J.E., Jr. (2007). Mechanisms of specificity in protein phosphorylation. Nat. Rev. Mol. Cell Biol. *8*, 530–541.

48. Boned Del Río, I., Young, L.C., Sari, S., Jones, G.G., Ringham-Terry, B., Hartig, N., Rejnowicz, E., Lei, W., Bhamra, A., Surinova, S., and Rodriguez-Viciana, P. (2019). SHOC2 complex-driven RAF dimerization selectively contributes to ERK pathway dynamics. Proc. Natl. Acad. Sci. USA *116*, 13330–13339.

49. Lv, J.M., Chen, L., Gao, Y., Huang, H., Pan, X.W., Liu, X., Chen, M., Qu, F.J., Li, L., Wang, J.K., et al. (2018). PPP5C promotes cell proliferation and survival in human prostate cancer by regulating of the JNK and ERK1/2 phosphorylation. OncoTargets Ther. *11*, 5797–5809.

50. Schuster, S., and Feldstein, A.E. (2017). NASH: novel therapeutic strategies targeting ASK1 in NASH. Nat. Rev. Gastroenterol. Hepatol. *14*, 329–330.

51. Wang, P.X., Ji, Y.X., Zhang, X.J., Zhao, L.P., Yan, Z.Z., Zhang, P., Shen, L.J., Yang, X., Fang, J., Tian, S., et al. (2017). Targeting CASP8 and FADD-like apoptosis regulator ameliorates nonalcoholic steatohepatitis in mice and nonhuman primates. Nat. Med. *23*, 439–449.

52. Dickson, I. (2020). No anti-fibrotic effect of selonsertib in NASH. Nat. Rev. Gastroenterol. Hepatol. *17*, 260.

53. Harrison, S.A., Wong, V.W.S., Okanoue, T., Bzowej, N., Vuppalanchi, R., Younes, Z., Kohli, A., Sarin, S., Caldwell, S.H., Alkhouri, N., et al.; STELLAR-3 and STELLAR-4 Investigators (2020). Selonsertib for patients with bridging fibrosis or compensated cirrhosis due to NASH: results from randomized phase III STELLAR trials. J. Hepatol. *73*, 26–39.

54. Noureddin, M., Mato, J.M., and Lu, S.C. (2015). Nonalcoholic fatty liver disease: update on pathogenesis, diagnosis, treatment and the role of S-adenosylmethionine. Exp. Biol. Med. *240*, 809–820.

55. Teo, G., Kim, S., Tsou, C.C., Collins, B., Gingras, A.C., Nesvizhskii, A.I., and Choi, H. (2015). mapDIA: preprocessing and statistical analysis of quantitative proteomics data from data independent acquisition mass spectrometry. J. Proteonomics *129*, 108–120.

56. MacLean, B., Tomazela, D.M., Shulman, N., Chambers, M., Finney, G.L., Frewen, B., Kern, R., Tabb, D.L., Liebler, D.C., and MacCoss, M.J. (2010). Skyline: an open source document editor for creating and analyzing targeted proteomics experiments. Bioinformatics *26*, 966–968.

57. Choi, M., Chang, C.Y., Clough, T., Broudy, D., Killeen, T., MacLean, B., and Vitek, O. (2014). MSstats: an R package for statistical analysis of quantitative mass spectrometry-based proteomic experiments. Bioinformatics *30*, 2524–2526.

58. Stachowski, M.J., Holewinski, R.J., Grote, E., Venkatraman, V., Van Eyk, J.E., and Kirk, J.A. (2018). Phospho-proteomic analysis of cardiac dyssynchrony and resynchronization therapy. Proteomics *18*, e1800079.

59. Röst, H.L., Rosenberger, G., Navarro, P., Gillet, L., Miladinović, S.M., Schubert, O.T., Wolski, W., Collins, B.C., Malmström, J., Malmström, L., and Aebersold, R. (2014). OpenSWATH enables automated, targeted analysis of data-independent acquisition MS data. Nat. Biotechnol. *32*, 219–223.

60. Reiter, L., Rinner, O., Picotti, P., Hüttenhain, R., Beck, M., Brusniak, M.Y., Hengartner, M.O., and Aebersold, R. (2011). mProphet: automated data processing and statistical validation for large-scale SRM experiments. Nat. Methods *8*, 430–435.

61. Röst, H.L., Liu, Y., D'Agostino, G., Zanella, M., Navarro, P., Rosenberger, G., Collins, B.C., Gillet, L., Testa, G., Malmström, L., and Aebersold, R. (2016). TRIC: an automated alignment strategy for reproducible protein quantification in targeted proteomics. Nat. Methods *13*, 777–783.

62. Eng, J.K., Jahan, T.A., and Hoopmann, M.R. (2013). Comet: an open-source MS/MS sequence database search tool. Proteomics *13*, 22–24.

63. Craig, R., and Beavis, R.C. (2004). TANDEM: matching proteins with tandem mass spectra. Bioinformatics *20*, 1466–1467.

64. MacLean, B., Eng, J.K., Beavis, R.C., and McIntosh, M. (2006). General framework for developing and evaluating database scoring algorithms using the TANDEM search engine. Bioinformatics *22*, 2830–2832.

65. Keller, A., Nesvizhskii, A.I., Kolker, E., and Aebersold, R. (2002). Empirical statistical model to estimate the accuracy of peptide identifications made by MS/MS and database search. Anal. Chem. *74*, 5383–5392.

66. Schilling, B., Rardin, M.J., MacLean, B.X., Zawadzka, A.M., Frewen, B.E., Cusack, M.P., Sorensen, D.J., Bereman, M.S., Jing, E., Wu, C.C., et al. (2012). Platform-independent and label-free quantitation of proteomic data using MS1 extracted ion chromatograms in skyline: application to protein acetylation and phosphorylation. Mol. Cell. Proteomics *11*, 202–214.

STAR★METHODS

KEY RESOURCES TABLE

REAGENT or RESOURCE	SOURCE	IDENTIFIER
Antibodies		
Rabbit polyclonal anti-catalase	Abcam	Cat# ab16731; RRID:AB_302482
Rabbit monoclonal anti-VDAC1/porin + VDAC2	Abcam	Cat# ab154856; Clone [EPR10852(B)]; RRID:AB_2687466
Biological samples		
Human NAFLD tissues	Biobank of the Fatty Liver Program at Cedars-Sinai Medical Center	IRB# Pro00042709
Chemicals, peptides, and recombinant proteins		
S-adenosylmethionine (SAMe)	Gnosis SRL, Cairate, Italy, available via Jarrow Industries, CA	Batch code # 0-S01 CAS: 29908-03-0
Critical commercial assays		
Triglyceride Colorimetric Assay Kit	Cayman Chemicals, MI	Cat# 10010303
ALT activity assay	Sigma	Cat# MAK052
AST colorimetric assay kit	Cayman Chemicals, MI	Cat# 701640
Deposited data		
Panorama (https://panoramaweb.org/Mat1a_NASH.url	This paper	ProteomeXchange ID: PXD022122
Panorama (https://panoramaweb.org/Larp1.url)	Published work (Ramani et al. 2022[18])	ProteomeXchange ID: PXD020015
Experimental models: Organisms/strains		
Mouse: *Mat1a*$^{-/-}$ KO male mice, C57BL/6 strain	Our published work (Lu et al., 2001[9])	N/A
Software and algorithms		
MapDIA software version v.1.1	Teo et al., 2015[55]	
Skyline software-Skyline-daily (64-bit) 20.1.1.83 (d7f345585)	MacLean et al., 2010[56]	
MSSTATs software suite v3.2.2	Choi et al., 2014[57]	

RESOURCE AVAILABILITY

Lead contact

Information regarding this work and requests for resources and reagents should be directed to and will be fulfilled by the lead contact, Jennifer E. Van Eyk (Jennifer.VanEyk@cshs.org).

Materials availability

This study did not generate unique reagents.

Data and code availability

- Phospho-peptide quantification data have been deposited on panorama (https://panoramaweb.org/Mat1a_NASH.url) and will be shared by the lead contact upon request. The ProteomeXchange ID is listed in the key resources table.
- Published dataset containing the phospho-proteomics data from *Mat1a*$^{-/-}$ animals with NASH treated with SAMe administration is available at https://panoramaweb.org/Larp1.url. (Ramani et al., 2022). The ProteomeXchange ID is listed in the key resources table.
- This paper does not report original code.

EXPERIMENTAL MODEL AND SUBJECT DETAILS

Animals

Four-month-old *Mat1a*$^{-/-}$ male mice were given vehicle (water, n = 4) or SAMe (in the form of disulfate p-toluene sulfonate dried powder provided by Gnosis SRL (Cairate, Italy), 100 mg/kg/day, n = 4) orally by gavage for one week before sacrificing. Age-matched wild-type male sibling littermates were also treated with vehicle for the same duration (n = 4). Animals were bred, maintained, and cared for as per National Institutes of Health (NIH) guidelines, and protocols were approved by the Institutional Animal Care and Use Committee of Cedars-Sinai Medical Center, Los Angeles, CA. Eight-month-old *Mat1a*$^{-/-}$ male mice (in C57Bl/6 background) with increased levels of liver transaminases and fat accumulation on ultrasound were given vehicle (water, n = 6) or SAMe (Abbott, Chicago, IL; 30 mg/kg/day, n = 5) orally by gavage for 8 weeks before sacrificing. Age-matched wild-type male sibling littermates showing normal serum liver transaminases and ultrasound were also treated with vehicle for the same duration (n = 6). Animals were bred and housed in the CIC bioGUNE animal unit, accredited by the Association for Assessment and Accreditation of Laboratory Animal Care International (AAALAC). After harvest, livers from all animals were briefly washed in ice cold PBS containing phosphatase inhibitor cocktail (Roche), snap-frozen in liquid N_2, and stored at −80C until further processing.

Human tissues

De-identified human NAFLD tissues were procured from the Biobank of the Fatty Liver Program at Cedars-Sinai Medical Center (NAFLD repository IRB# Pro00042709). Samples were processed for phospho-proteomics and proteomics analysis as explained in the method details section. Clinical characteristics are listed in Table 2.

METHOD DETAILS

Sample preparation for proteomic analysis

Frozen livers were ground while frozen in a liquid N_2 cooled cryohomogenizer (Retsch). 8M urea and 100 mM TRIS-HCL, pH 8.0 was added the liver power, ultrasonicated (QSonica) at 4°C for 10 minutes with 10 second repeating on/off intervals and centrifuged at 16,000 × g for 10 minutes at 4°C. To the soluble fraction, DTT (15 mM) was added for 1h at 37°C, followed sequentially by iodoacetamide (30 mM) for 30 minutes at room temperature in the dark, diluted to a final concentration of 2M Urea with 100 mM TRIS-HCL, pH 8.0 and Trypsin/Lys-C mix (Promega) at a 1:40 dilution for 16 hours on a shaker at 37°C. Each sample was de-salted using HLB plates (Oasis HLB 30 μm, 5 mg sorbent, Waters) and eluted in 300 μL of 80% ACN, 5% TFA, 1 m glycolic acid.

Titanium dioxide phospho enrichment

Titanium Dioxide (TiO2) phosphorylation affinity enrichment was performed as previously described.[58] Briefly, 400 μg of digested peptides were incubated in 50 μL titanium dioxide (TiO2) slurry (30 mg/mL, Glygen Corp, Columbia, MD) at room temperature on a shaker for 16 hrs. TiO2 beads were washed twice with 200 μL of 80% ACN, 5% TFA, once with 200 μL of 80% ACN, 0.1% TFA, and eluted in 180 μL of 30% ACN/ 1% NH4OH and neutralized with 200 μL of 10% FA. Samples were then desalted on Oasis HLB μ-elution plates (Waters) and eluted in 80% ACN, 0.1% FA, dried in Speedvac, then resuspended in 0.1% FA for LC–MS/MS analysis.

Quantitation of individual specimen by DIA-MS

Tryptic peptide assay library was created by DDA acquisitions of 5 strong Cation Exchange (SCX) fractions from glycine N-methyltransferase knockout (*Gnmt*$^{-/-}$) mouse livers was we described[44] was used for DIA analysis. Peak group extraction and FDR analysis was done as we outlined.[44] Raw intensity data for peptide fragments was extracted from DIA files using the open source openSWATH workflow against the sample specific peptide assay.[59] Then, retention time prediction was made using the Biognosys iRT Standards spiked into each sample. Target and decoy peptides were then extracted. scored and analyzed using the mProphet algorithm to determine scoring cut-offs consistent with 1% FDR .[60] Peak group extraction data from each DIA file was combined using the 'feature alignment' script, which performs data alignment and modeling analysis across an experimental dataset.[61] Finally, all duplicate peptides were removed from the dataset to ensure that peptide sequences are proteotypic to a given protein in our FASTA database.

DIA-MS data normalization, quantitation, and visualization

The total ion current (TIC) associated with the MS2 signal across the chromatogram was calculated for normalization using in-house software. This 'MS2 Signal' of each file was used to adjust the transition intensity of each peptide in a corresponding file. Normalized transition-level data was then processed using the mapDIA software to obtain total protein quantity and perform pair-wise comparisons between groups at the peptide level.[55] For phospho-proteomics analysis, to obtain the ratio of phosphorylation when compared to total protein quantity (Phospho/Total), the intensity of each unique phospho-peptides was divided by its corresponding protein quantity.

Phospho enrichment database searches and quantification

DDA files were converted to mzXML and searched through the Trans Proteomic Pipeline (TPP) using 3 algorithms, (1) Comet,[62] (2) X!tandem! Native scoring,[63] and (3) X!tandem! K-scoring[64] against a reviewed, mouse canonical protein sequence database, downloaded from the Uniprot database on January 24th, 2019, containing 17,002 target proteins and 17,002 randomized decoy proteins. Target-decoy modeling of peptide spectral matches was performed with peptide prophet[65] and peptides with a probability score of >95% from the entire experimental dataset were imported into Skyline software[56] for quantification of precursor extracted ion intensities (XICs). Precursor XICs from each experimental file were extracted against the Skyline library, and peptide XICs with isotope dot product scores>0.8 were filtered for final statistical analysis of proteomic differences.[66] Raw peptide intensities were used to calculate pairwise comparisons between experimental groups using the linear mixed effects model built into the open sources MSSTATs (v3.2.2) software suite.[57] Peptide abundance differences with a p-value <0.05 were considered significantly different. The Skyline documents containing precursor XICs from each experimental file are available at Panorama. Phospho-peptide quantification files are uploaded on panorama (https://panoramaweb.org/Mat1a_NASH.url, Proteome Exchange ID: PXD022122). Additionally, our recently published dataset containing the phospho-proteomics data from *Mat1a*$^{-/-}$ animals with NASH treated with SAMe administration is available at https://panoramaweb.org/Larp1.url.[18]

Triglyceride measurement

Liver triglycerides were extracted and quantified using the triglyceride colorimetric assay kit (Cayman Chemicals, MI) following the manufacturer's protocol. Briefly, tissues and triglyceride standards from the kit were solubilized in a NP-40-substitute buffer. These were further treated with an enzyme mixture containing lipase, glycerol kinase, glycerol oxidase and peroxidase to sequentially generate glycerol, glycerol-3 phosphate, dihydroxyacetone phosphate + H_20_2. The H_20_2 reacted with the peroxidase in the presence of 4-aminoantipyrine and N-ethyl-N-(3'-sulfopropyl)-m-anisidine to produce a brilliant purple quinoneimine dye whose absorbance could be measured at a wavelength of 530–550 nm. The absorbance of the triglyceride standards was plotted against their amount in milligrams and the standard curve was used to determine the amount of triglyceride in the tissue samples. Data are represented as mg of triglyceride/gm of tissue.

ALT/AST assay

Serum ALT assay was measured using the ALT activity assay kit according to the manufacturer (Sigma). Serum AST levels were measured by the AST colorimetric assay kit according to the manufacturer's protocol (Cayman Chemicals).

H&E staining

Paraffin-embedded liver tissues were stained with hematoxylin and eosin (H&E) using the core services provided by the liver histology core of the University of Southern California research center for liver diseases (NIH grant P30 DK048522).

Hepatic peroxisome and mitochondria staining

Liver tissues were fixed in neutral buffered 10% formalin solution (Sigma-Aldrich, HT501128-4L) embedded in paraffin and cut into 5-μm sections. Liver sections were deparaffinized with Histo-Clear I solution (Electron Microscopy Sciences, 64110-01) and hydrated through decreasing concentration of alcohol solutions. For catalase (peroxisomal marker) and VDAC1/2 (mitochondrial marker) staining, sections were unmasked 20 minutes at 600 W in a microwave with citrate buffer, pH 6.0. Samples were then blocked for 10 min with 3% H_2O_2 followed by 30 min with 2.5% normal goat serum. Sections were further incubated overnight at 4°C

with primary antibodies (1:100 dilution) (catalase ref: ab16731; VDAC1/2, ab154856, Abcam) followed by 30 minutes of incubation with goat anti-Rabbit IgG Alexa Fluor™ 647 (for catalase staining) or goat anti-Rabbit IgG Alexa Fluor™ 488 (for VDAC1/2 staining) (1:200 dilution) (Thermo Fisher Scientific). Samples were mounted with Fluoromount-G mounting medium with DAPI (Invitrogen). All images were captured using a Carl Zeiss Axioimager D1 fluorescent microscope and quantified for number and size of peroxisome and mitochondria using Image J software.

QUANTIFICATION AND STATISTICAL ANALYSIS

Normalized transition-level data was processed using the mapDIA software to obtain total peptide and protein quantities, remove data missingness (minimum 50% observations present per experimental group) and perform statistical analysis of pair-wise comparisons between the experimental groups at the protein and peptide level.[55] Differences between groups were identified by pair-wise comparisons using differential expression analysis based on a Bayesian latent variable model with Markov random field model as previously described.[55] Proteins/peptides were considered significantly different with the computed Bayesian FDR of less than 0.05.